Chapter 3

Variation of X-ray Spectral Index with Eddington Ratio

3.1 Introduction

AGN are known to emit X-rays as a result of physical processes active in the innermost regions near the central super-massive black hole. X-ray spectra of a typical AGN in the 2.0–10.0 keV range show primarily the signature of a power-law continuum and an iron line. At energies < 2 keV there is often a soft excess over the power-law emission. The power-law emission is widely considered as the outcome of inverse Compton scattering of thermally produced accretion disk seed optical/UV photons by a corona of hot electrons close to the disc [181–183]. However, the geometry and size of the corona as well as the physical mechanism governing the energy transfer between the two phases are not well understood.

While, the average value of photon index of the primary power-law for AGN has been found to be $\Gamma \sim 1.9$, there is a large variation with Γ ranging from 1.5–2.5 [184, 185]. For a given AGN, Γ varies as a function of time. Understanding the behaviour of Γ with other source properties is expected to give important insight into the nature of the radiative mechanism and the geometry of the inner regions.

3.2 Correlation Between Γ and Eddington Ratio

Previous studies have shown the existence of a correlation between the X-ray photon index Γ and the source flux [186–190]. For many Seyfert 1 AGNs, the power-law index shows significant variation and generally follows the trend of steeper Γ with increasing source intensity. During 1997, MCG 6-30-15 was observed with *RXTE* for a duration of 8 days ($\sim$ 910 ks). The range of Γ observed was 1.8–2.2 with flux variation of $\sim$ 3.3 in the energy band 2.0–10.0 keV. This observation showed a tight correlation between the photon index Γ and the source flux in the sense that the power-law steepens as the source gets brighter [191]. The steepening of Γ (range 1.89–2.34) with flux has also been observed in IRAS 13224-3809, where a 10 day long *ASCA* observation revealed a change in the power-law flux by a factor of $\sim$ 3.2 in the 2.0–10.0 keV range [192]. *RXTE* observed NGC 5548 on five occasions in 1998 during which a clear positive correlation between the photon index (range 1.75–1.93) and the 2.0–10.0 keV flux was seen with flux variation of $\sim$ 1.84 [193]. For the soft energy band (0.3–2.0 keV), similar trend between photon index (range 1.7–2.0) and flux was observed for a 2 day long *BEPPOSAX* observation of 3C 120 with flux variation of $\sim$ 1.5 [194]. The Seyfert galaxy NGC 4151 was observed on seven occasions by *Ginga* during May 1987-January 1989 ($\sim$21 months). In this observation significant flux variation ($\sim$ 3) has been seen along with the correlation between the photon index and flux [195]. The 2009 *XMM-Newton* observation of Mrk 335 has also shown 'softer when brighter' property [196]. Table 3.1 lists these examples of AGNs for which the correlated spectral index variability with flux has been reported. In all the above examples of AGNs, the flux variation during the observations does not exceed a factor of $\sim$ 4.

Table 3.1: AGNs showing Γ–Flux relation

Object	Satellite	Exposure	Γ range	F_{max}/F_{min}	Energy Range	Ref.
MCG 6-30-15	RXTE	∼8 days	1.8-2.2	∼3.3	(2.0-10.0)	[191]
IRAS 13224-3809	ASCA	∼834 ks	1.89-2.34	∼3.2	(2.0-10.0)	[192]
NGC 5548	RXTE	∼243 ks	1.75-1.93	∼1.84	(2.0-10.0)	[193]
3C 120	BEPPOSAX	∼2 days	1.7-2.0	∼1.5	(0.3-2.0)	[194]
NGC 4151	EXOSAT	∼21 months	∼1.4-1.7	∼3	(2.0-10.0)	[195]
Mrk 335	XMM-Newton	∼200 ks	1.8-2.1	∼2.15	(0.3-10.0)	[196]

Studies of a sample of AGNs have also provided evidence that there is significant positive correlation between the X-ray photon index and the bolometric Eddington ratio, $\lambda = L_{Bol}/L_{Edd}$, where L_{Edd} is the Eddington luminosity [197–200]. With larger samples involving sources with higher redshifts and greater luminosities, it was observed that the hard X-ray photon index correlates with the bolometric Eddington ratio when $\lambda \gtrsim 0.01$ [200–207] but when $\lambda < 0.01$, especially for low-luminosity AGNs, anti-correlation is seen between Γ and λ [208–211]. In general, there have been several studies to investigate the relation between the photon index and λ for different samples of AGN [212, 213]. Studies incorporating *ROSAT* and *ASCA* observations showed the correlation between Γ and FWHM of the Hβ emission line [192, 214, 215].

3.3 NLS1 Galaxy

NLS1 form a subset of AGN which exhibit exceptional features in terms of emission-line and continuum properties. Seyfert1 galaxies show a large range in the width of their optical emission lines. The FWHM of the (Hβ) line of Seyfert1 galaxies is found to be in the range $\sim$ 1000 – 10000 km s^{-1}. Seyfert1 galaxies which have FWHM (Hβ) $\lesssim$ 2000 km s^{-1}, [O III]/Hβ flux ratio <3.0 and prominent optical Fe II emission are called Narrow–Line Seyfert1 Galaxies [216–218]. AGN with FWHM > 2000 km s^{-1} are generally known as Broad line Seyfert1 (BLS1) galaxies.

NLS1 also show a number of other extreme properties in X-rays e.g., strong soft excess emission below 1 keV, steep 2.0–10.0 keV power-law continuum and very rapid and large X-ray variability [220, 221]. The 2.0–10.0 keV spectrum of classical BLS1s can be fitted with a power law with a photon index Γ=1.73±0.05 [184, 222, 223]. But in case of NLS1s, photon index is significantly steep (Γ=2.19±0.10) [220]. The photon index of NLS1s is found to be anti-correlated with the FWHM of Hβ line [214, 224]. NLS1 often have strong infrared emission [225]. NLS1s are generally radio-faint but in very fewer cases they are found as radio-loud [226, 227]. NLS1 galaxies show larger variability in X-rays than BLS1s and their soft excess is stronger. Again the emission-line metallicity indicator (N V/C IV)

is much stronger in NLS1s [228]. It has also been proposed that NLS1s are an evolutionary phase of AGN [229].

Their X-ray spectra often present complex behaviour with the presence of cold and ionised absorption, partial covering and reflection components ([230] and references therein). Also NLS1 galaxies as a class follow the $M_{BH} - \sigma_*$, relation if the widths of emission lines not strongly affected by outflow components are used as a surrogate for σ_* [231], where σ_* is variance.

Recent observations and surveys have pointed towards the presence of smaller black hole masses in NLS1 galaxies [232, 233] and which could possibly represent an important connection with the less explored intermediate mass black holes. It is believed that the extreme X-ray and other observed properties of NLS1 galaxies may be due to an extreme value of a fundamental physical parameter related to the accretion process. This fundamental parameter is most likely to be the accretion rate relative to the Eddington rate. This is well supported by more recent studies, theoretical considerations and by black hole mass estimates from optical emission-line and continuum measurements that NLS1 are accreting close to their Eddington rates [215, 234–238] and hence should be considered important testbeds of accretion models. Recent X-ray study of NLS1 using an optically selected SDSS sample have shown that some NLS1 show steep X-ray spectra and strong Fe II emission while some do not. In this study, a strong correlation was also found between Γ and the luminosity at 1 keV, L_{1keV} suggesting differences in L_{Bol}/L_{Edd} among the NLS1s in the sample [239, 240]. Due to all these extreme and ambiguous properties, NLS1 as a special class of AGN seem to challenge the Unified model and need a more careful investigation.

3.4 Object Selection

There is a need to study the relation between spectral index and Eddington ratio spanning a larger range in L/L_{Edd}. This is provided by *XMM-Newton* data for the bright and highly variable NLS1 galaxy Mrk 335 and Ark 564. Both these two sources have been observed by almost all observatories. As the aim of the study is to investigate the dependence of power-law photon index with the X-ray

Eddington ratio for the combined EPIC pn spectra of Mrk 335 and Ark 564, so all available archive data have been selected, as observed by the *XMM-Newton* for both the objects. The list of observations are shown in Table 3.2. With this aim a comprehensive flux resolved spectral analysis have been done for the two sources.

Table 3.2: Observation log of Mrk 335 and Ark 564 by *XMM-Newton*

Mrk 335			
OBS. ID	Duration(s)	Date	Pile-up
0101040101	36910	2000-12-25	yes
0306870101	133251	2006-01-03	no
0510010701	22580	2007-07-10	no
0600540601	132315	2009-06-11	no
0600540501	82615	2009-06-13	no
Ark 564			
0006810101	34466	2000-06-17	no
0006810301	16211	2001-06-09	no
0206400101	101774	2005-01-05	no
0670130201	59500	2011-05-24	yes
0670130301	55900	2011-05-30	no
0670130401	63620	2011-06-05	no
0670130501	67300	2011-06-11	yes
0670130601	60900	2011-06-17	no
0670130701	64420	2011-06-25	no
0670130801	58200	2011-06-29	yes
0670130901	55900	2011-07-0	yes

3.4.1 Mrk 335

Mrk 335 (α=00hh 06m 19.5s, $\delta = +20^\circ\ 12'\ 10''$ [J2000.0]), also known as PG0003+199 is a nearby NLS1 galaxy at a redshift z=0.026 [241]. It has a well measured black hole mass of 1.4 $\times 10^7$ $M_\odot$ from reverberation mapping [242, 243]. Mrk 335 has

been observed by almost all X-ray satellites. It was first detected in X-rays by *UHURU* [244] and *Einstein* observation found it as a bright AGN [245]. Pounds et al. [246] using *EXOSAT* observations in the 0.1–10.0 keV band found strong X-ray excess and very high variability on timescales of 1–2 hour. The soft X-ray excess found in the *EXOSAT* spectrum was confirmed by *BBXRT* observations [247]. Turner et al. [247] reported the presence of a variable, ionized absorber as they observed Fe edge in *Ginga* data of Mrk 335. In the *ASCA* observation of this object, the presence of a strong soft excess without clear signature of edges or ionized absorption at low energies was reported [222, 223]. Evidence for a broad Fe line was also found from *ASCA* observation [248]. Ballantyne et al. [249] found a good fit to the entire 0.6–10.0 keV band *ASCA* spectrum with an ionized reflection model. Grupe et al. [250] using *ROSAT* data also observed strong soft X-ray excess in the spectrum of Mrk 335. *BeppoSAX* observation [251] found both a broad Fe line as well as a soft excess, but revealed a rather small Compton reflection component.

XMM-Newton observed Mrk 335 for the first time in 2000. Analysing the RGS data, an absorption edge at 0.54 keV due to Galactic oxygen was reported and the soft excess was described as a combination of bremsstrahlung emission and ionised reflection from the accretion disk [252]. The *XMM-Newton* observation was later reanalysed and a narrow absorption feature at 5.9 keV was found [241]. In 2006 January, *XMM-Newton* re-observed Mrk 335 for 133 ks which revealed a double-peaked Fe emission feature with peaks at 6.4 and 7.0 keV [253]. Larsson et al. [254] studied Mrk 335 using *Suzaku* data of 151 ks. They modelled the data using a power law and two reflectors in which an ionised, heavily blurred, inner reflector produces most of the soft excess, while an almost neutral outer reflector produces most of the Fe line emission. They also verified their model using the 2006 *XMM-Newton* data and did not see any correlation between photon index and power law flux. Subsequently a marginal trend, i.e., the source becomes softer with increasing count rate has been reported for the same data [196]. When observed by *XMM-Newton* in July 2007 for 22 ks, Mrk 335 was found to be in extremely low X-ray flux state [255]. The spectrum of this low flux state of Mrk 335 was explained by partial covering and blurred reflection models. *Swift* observation

also caught the object in a historical low X-ray flux state, with the flux having diminished by a factor of 30 compared to previous observations [256]. Mrk 335 was again observed by *XMM-Newton* in 2009 for 200 ks spread over two consecutive orbits. The X-ray continuum and timing properties have been described by using a blurred reflection model [257]. The 2009 *XMM-Newton* data have also been analysed by Grupe et al. [196] along with the *Swift* data. Partial absorption and blurred reflection models gives equally good fit to the spectrum.

The spectrum obtained from the 2013 *NuSTAR* observation has been described by the relativistically blurred reflection of X-rays originating from a compact corona within a few gravitational radii of the black hole [258]. With *XMM-Newton, Suzaku* and *NuSTAR* observations in between 2006 and 2013, Wilkins & Gallo [259] found evidence of evolving corona and jet–launching in Mrk 335.

Mrk 335 has been studied in other waveband also. Mrk 335 has been variable in the UV between 1978 and 1985 by a factor of two as shown by historic light curves from *IUE* and *HST* [260, 261]. Highly variable property of this AGN was also suggested in UBVRI photometry [262]. From combined observations in the UV, optical and infrared bands, spectrum with UV excess has been generated that can be fitted with a blackbody at 25,600 K [263, 264]. The UV and optical continuum of Mrk 335 has been described by an accretion disk spectrum with a Lyman edge feature [265]. *Swift* observation in 2007 suggest that the UV variation of Mrk 335 is of the order of 0.2 magnitude [256]. In the *HST COS* spectra broad absorption lines of C IV that is intrinsic to the AGN and blueshifted by a velocity roughly comparable to the X-ray outflow has been found [266].

3.4.2 Ark 564

At a redshift z=0.02469 [267], Ark 564 is the brightest NLS1 galaxy in the (2.0–10.0) keV range with luminosity $L_{(2-10)keV} = 2.4\times10^{43}$ erg s^{-1} [282]. Ark 564 (α=22hh 42m 39.3s, $\delta = +29°43'.31''$ [J2000.0]) shows large amplitude variations on short time scales [268].

In the 2000 and 2001 *XMM-Newton* observations of Ark 564, Vignali et al. [269] reported edge-like feature in the EPIC data at ~ 0.73 keV and interpreted as O VII K absorption edge. 50 ks *Chandra* observation of Ark 564 revealed a steep

power-law ($\Gamma = 2.54 \pm 0.06$) above 2 keV and an edge-like absorption feature at 0.712 keV [270]. They found evidence for two phase warm absorber and fit the soft excess below 1.5 keV with a blackbody, of temperature 0.124 ± 0.003 keV. Spectra obtained from *ROSAT, ASCA* and *BeppoSAX* revealed an emission like feature at $\sim$ 1 keV [271–273] Comastri et al. [273] from *BeppoSAX* observations detected a narrow iron emission line at $\sim$6.8 keV and an absorption edge at $\sim$9.5 keV. Another edge at 8.5 keV was reported in a combine *ASCA* and *RXTE* data which was described as reflection from strongly irradiated disc [274]. The $\sim$ 100 ks 2005 *XMM-Newton* observation of Ark 564 has been described as either a power law and two blackbodies or a relativistically blurred photo ionized disk reflection model [275]. They modelled the MOS and pn spectra with either a power-law of slope 2.43 $\pm$ 0.03 and two blackbodies, with kT $\sim$0.15 and $\sim$0.07 keV. They also detected an absorption line at $\sim$8.1 keV which they assumed as FeXXVIK α line. Dewangan et al.[276] also analysed the same 2005 data and found two warm absorber phases. Along with the EPIC data they also analysed the RGS spectrum and find two warm absorber phases. Analysing combined *XMM–Newton* RGS spectrum of Ark 564 obtained from 2000 to 2005 Smith et al. [277] found three separate phases of photoionized X-ray absorbing gas. During 2011, Akn 564 has been observed by *XMM-Newton* for eight occasions. Legg et al. [278] confirmed a significant soft lag between the 0.3–1.0 keV and 4.0–7.5 keV bands and suggest a distant reflection origin. Gupta & Mathur [279] analysed the 250 ks *Chandra* archival 2008 observations of Ark 564 made with both HETGS and LETGS. They suggest two warm absorbers with two different ionization states for the high resolution X-ray spectrum both with moderate outflow velocities and low line of sight column densities.

Ark 564 has been studied across all wavebands [280, 281]. It was observed for a period of $\sim$35 days in 2000 by *ASCA*. The soft excess and power-law components have been found to be varying differently on a timescale of weeks with the soft excess emission varying by a factor of $\sim$6 compared to a factor of $\sim$4 in the power-law component [282]. No time lags between any energy bands was found [283] but with the same *ASCA* data in the power spectrum of Ark 564, slope break ("-1 to -2") was reported [284]. Using *RXTE* observation Pounds et al. [285] also

detected low frequency power spectral density (PSD) slope break at $\sim$1/13 days^{-1}. Analysing UV data from *HST STIS*, Crenshaw et al. [286] detected absorption lines of Lyα, NV, CIV, Si IV and Si III centred at a radial velocity of –190 km s^{-1}. Using a 63 ks *FUSE* observation, Romano et al. [287] detected strong emission in the O VI $\lambda\lambda$ 1032, 1038 resonance doublet. They also observed absorption troughs due to Lyman series of hydrogen, O VI, and C III λ977 at velocities near the systemic redshift of Ark 564. Collier et al. [288] reported a long ($\sim$ 2 months) monitoring of this object with *HST*. They found a low value of (by a factor of 3 than typical Seyfert1) fractional variability amplitude of the continuum variations between 1365 and 3000 Å.

3.5 Data Reduction

The observation data files (ODFs) were downloaded from the XMM-Newton Science Archive (XSA). Due to the high signal to noise ratio and better efficiency, observations by the EPIC pn camera are only considered. For the analysis, all the available archival data of Mrk 335 and Ark 564 observed by the *XMM-Newton* satellite are used. The list of observations are shown in Table 3.2. The *XMM-Newton* ODF have been processed in the standard way using the SAS version 12.0. After processing these ODFs to event lists, we further filtered these event lists. The data were cleaned for high background flares and were selected using the conditions PATTERN $\leqq$ 4 and FLAG == 0. We have checked for pile-up in all cases using SAS task *epatplot* and found that for both the sources some observations are affected by pile-up (Table 3.2). We reduced the pile-up by excluding the innermost source emission using an annular region as considered by Legg et al. [278]. Except for the pile-up affected observations, the source spectra have been extracted from circular regions of radius 35 arcsec centred on the maximum source emission. The redistribution matrices and auxiliary response files were created by the SAS task *especget*. Spectra were grouped such that each bin contained at least 30 counts. Spectral fits to the data were performed with XSPEC version 12.8.0 [289]. The background subtracted light curves have been produced with the tool *EPICLCCORR* which are binned with 400 s bins.

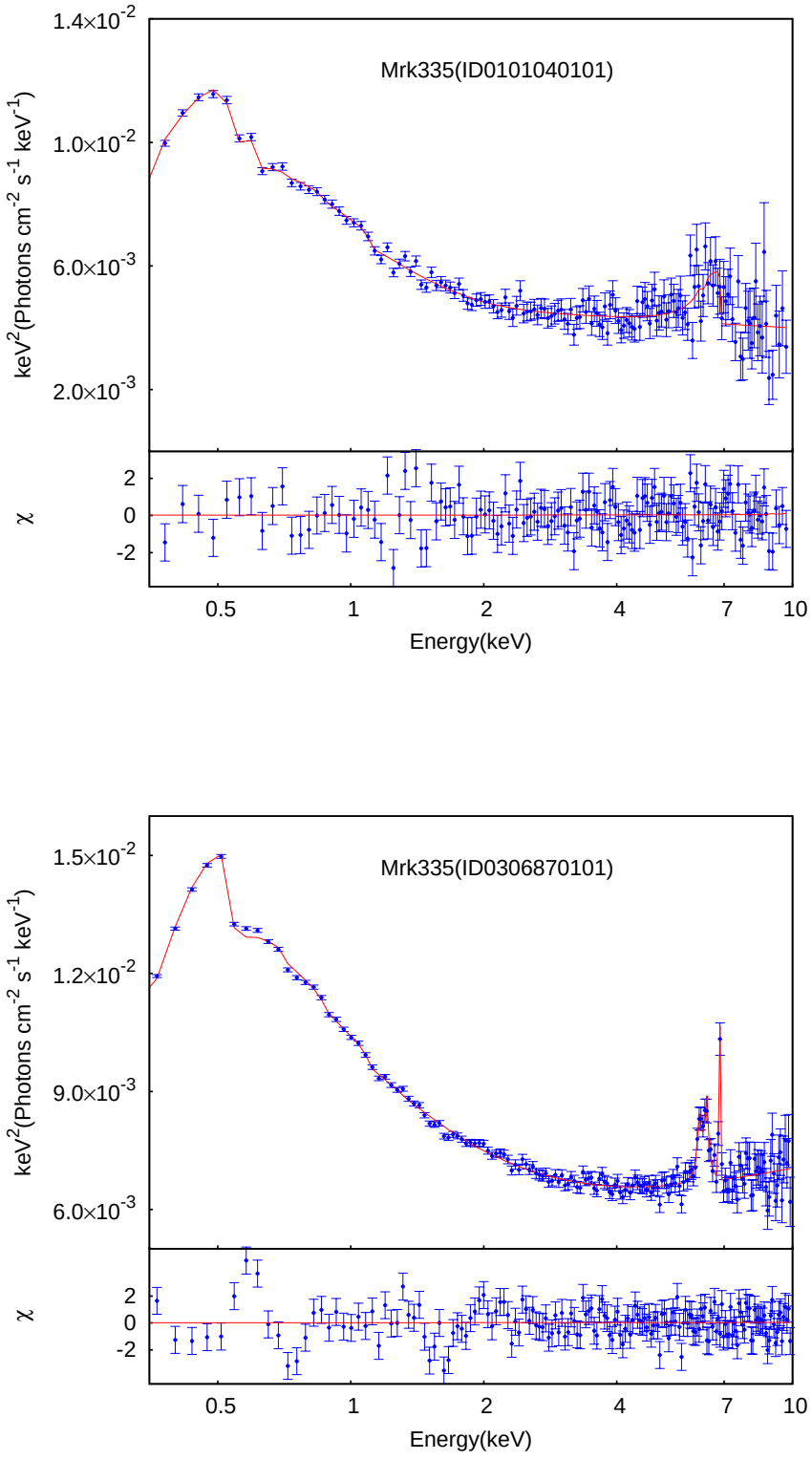

Figure 3.1: EPIC PN unfolded spectra and delchi of Mrk 335 for 0101040101 and 0306870101 observations.

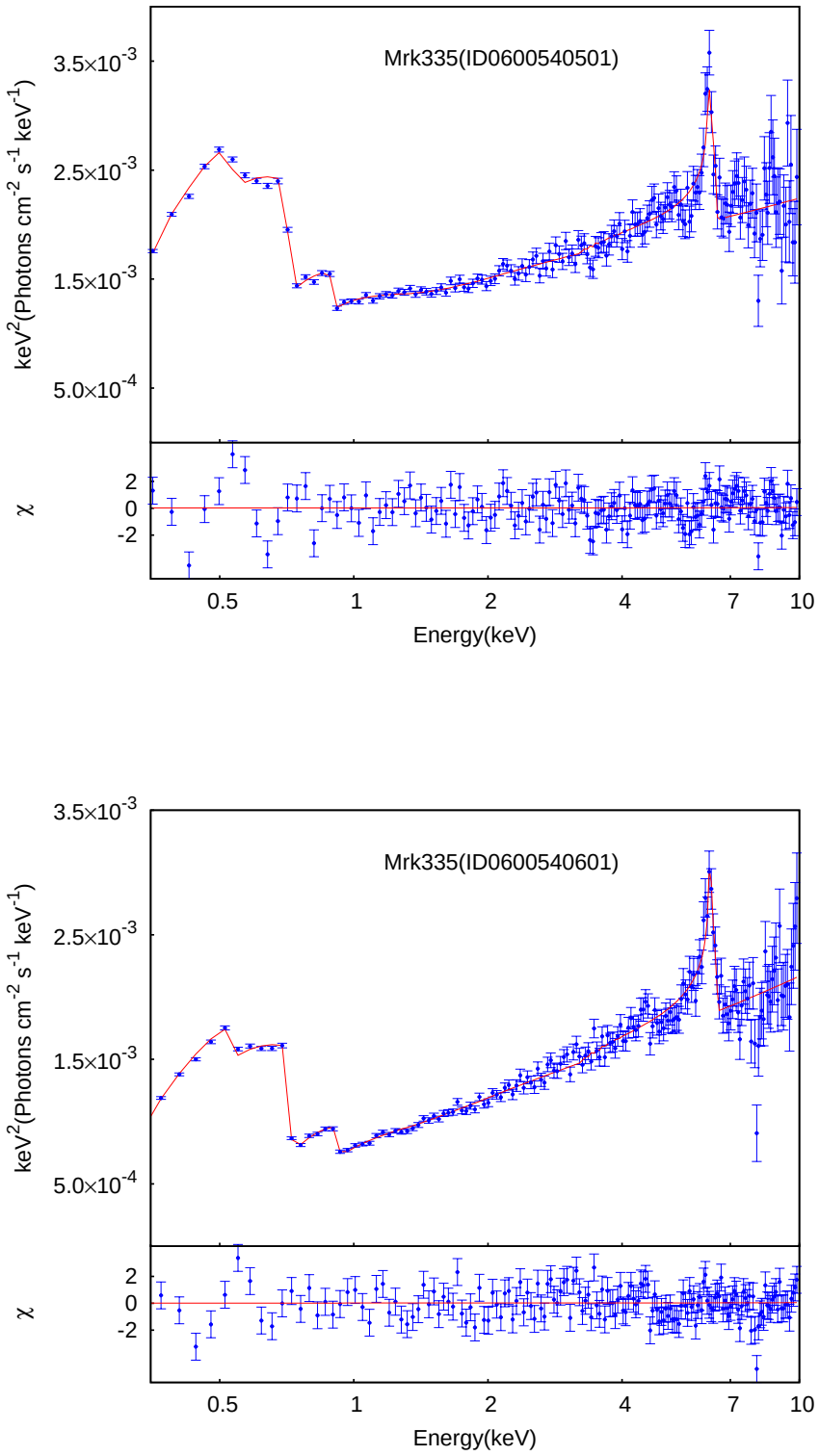

Figure 3.1: continued (ID0600540501 & ID0600540601)

3.6 Phenomenological Model

As is the case for many AGN, the time-averaged X-ray spectra of Mrk 335 and Ark 564 as observed by XMM-Newton are complex (Figures 3.1 & 3.2). In this

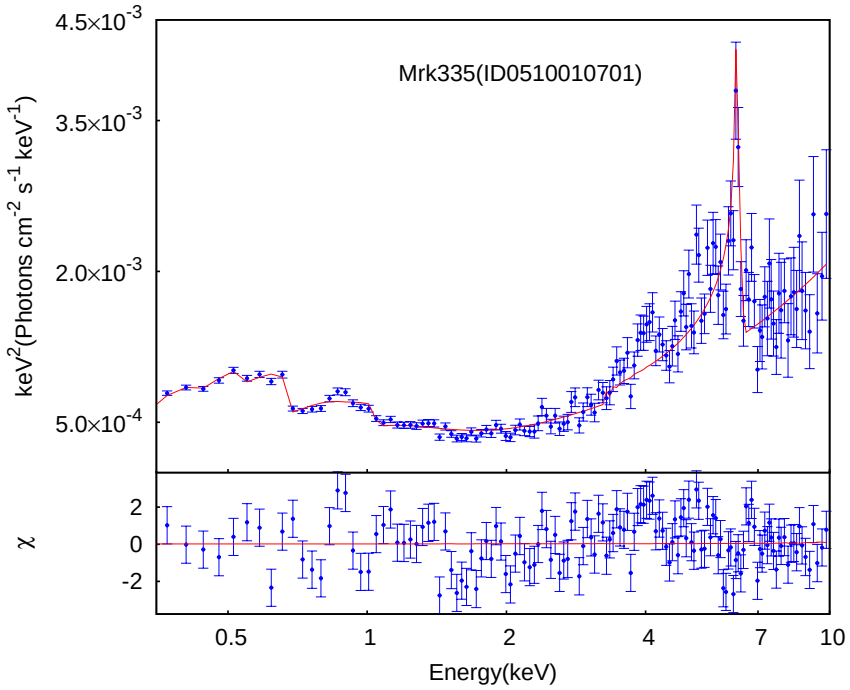

Figure 3.1: continued (ID0510010701)

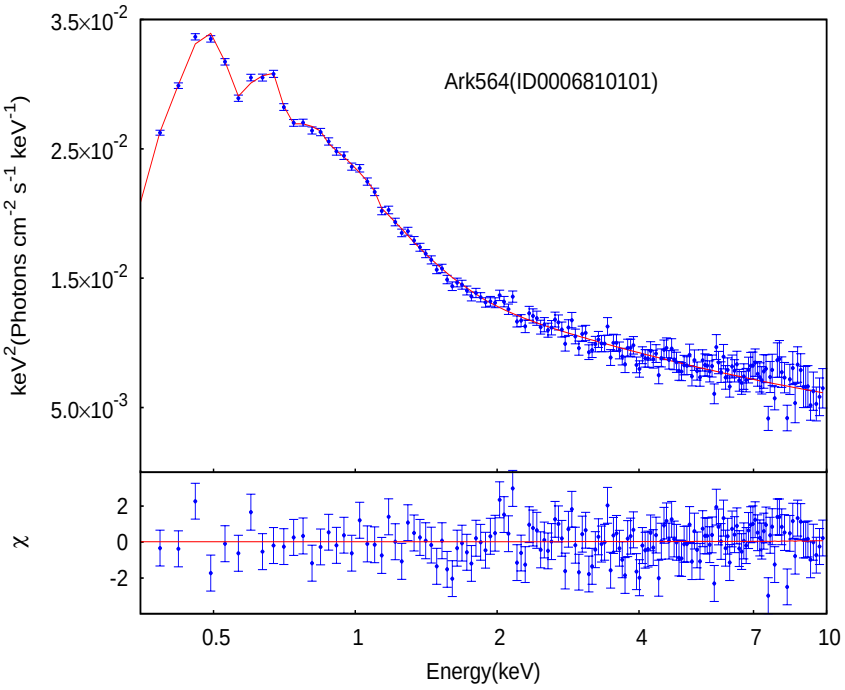

Figure 3.2: EPIC PN unfolded spectra and delchi of Ark 564 for ID0006810101.

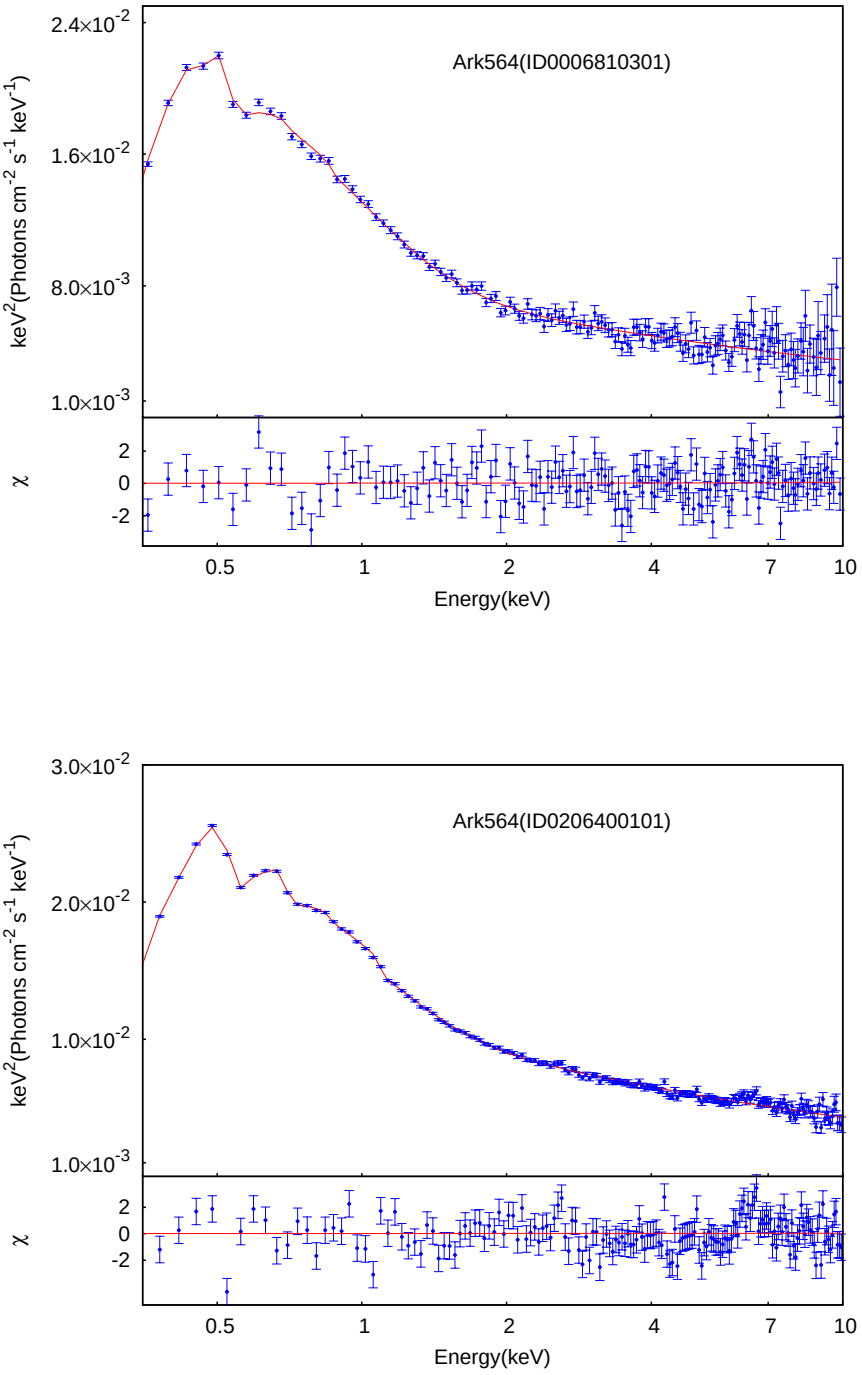

Figure 3.2: continued (ID0006810301 & ID0206400101.)

work, we have not attempted to fit the spectrum in detail, but to get a first order approximation which describes its overall shape. We model the spectrum in the 0.3–10.0 keV range using an intrinsically absorbed dual Comptonization model. One Comptonization component to describe the soft excess and the other for the hard X-ray continuum. Galactic absorption is taken to be N_H=3.99×10^{20} cm^{-2} for

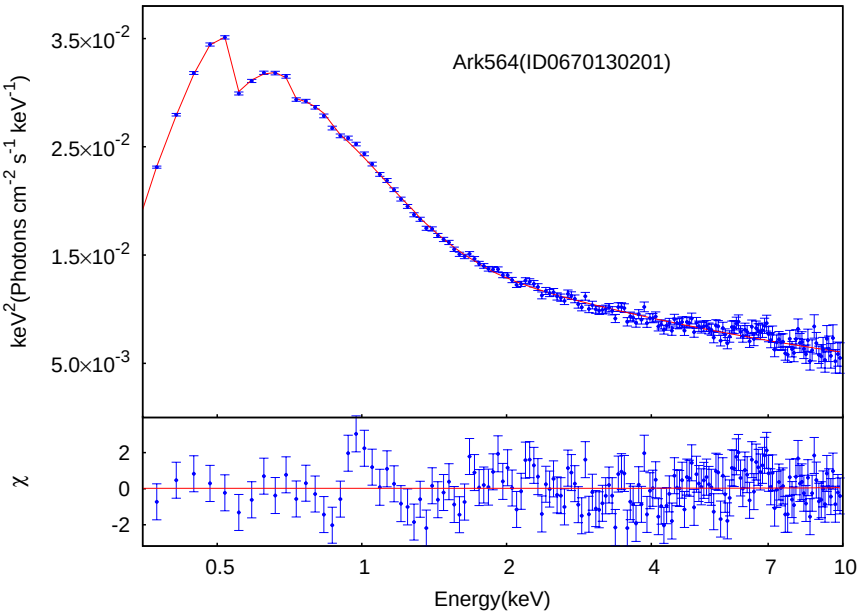

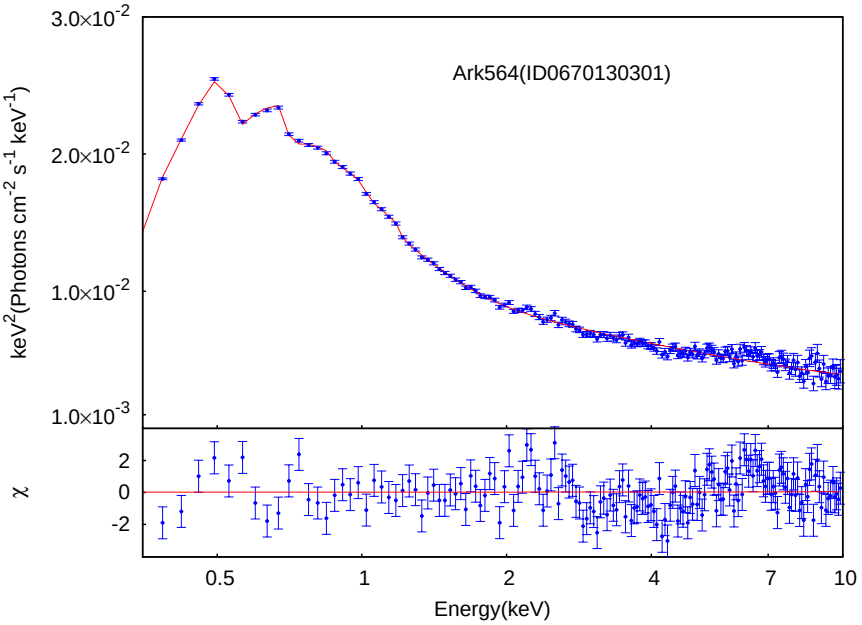

Figure 3.2: continued (ID0670130201 & ID0670130301.)

Mrk 335 and N_H=5.34×10^{20} cm^{-2} for Ark 564 [290]. The soft excess is described by a Comptonized component represented by the XSPEC model "nthcomp" [291, 292]. A second Comptonization model for the hard X-ray emission, is represented by the XSPEC convolution model "Simpl" [293] acting on the first Comptonization model "nthcomp". Thus, in this description, the first Comptonization component

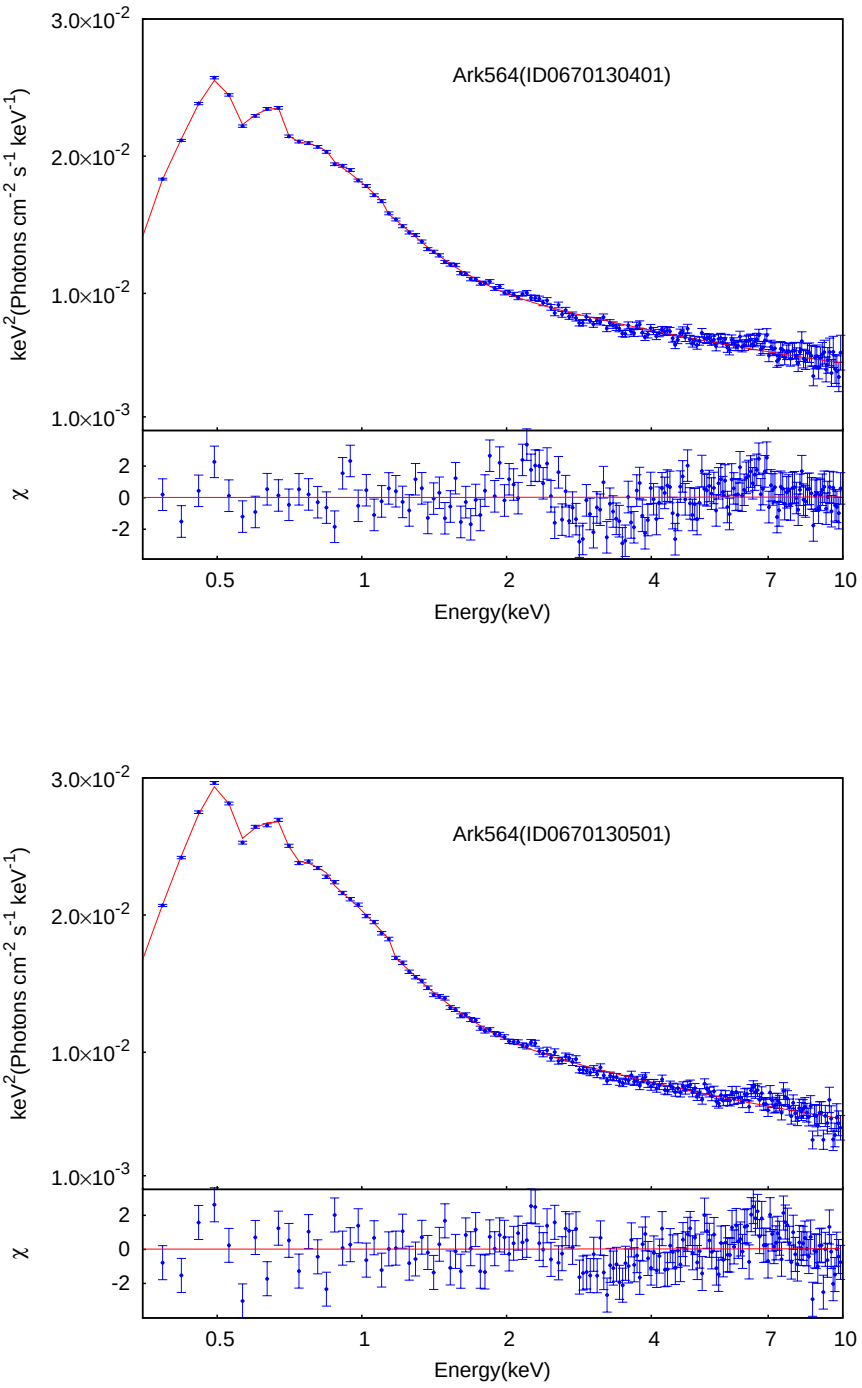

Figure 3.2: continued (ID0670130401 & ID0670130501.)

which gives rise to the soft excess, is the origin of the seed photons for the second Comptonization component giving the hard X-ray continuum.

For Mrk 335 there are clear residuals at around ~ 6 keV signifying the presence of a broad Iron line which we modelled using the "diskline" [294]. The inner radius of the line emitting region R_{in} is fixed at $6r_g$ and the outer radius r_{out} is

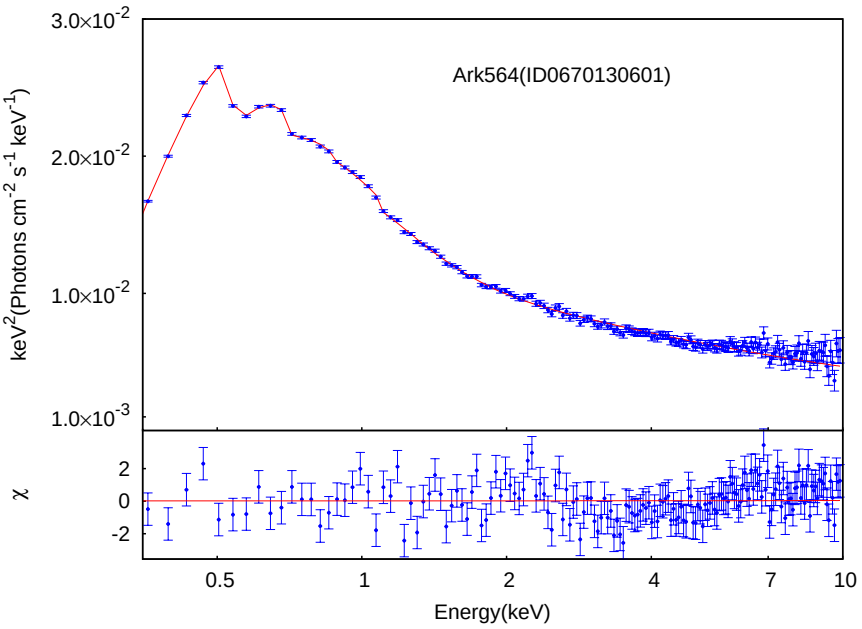

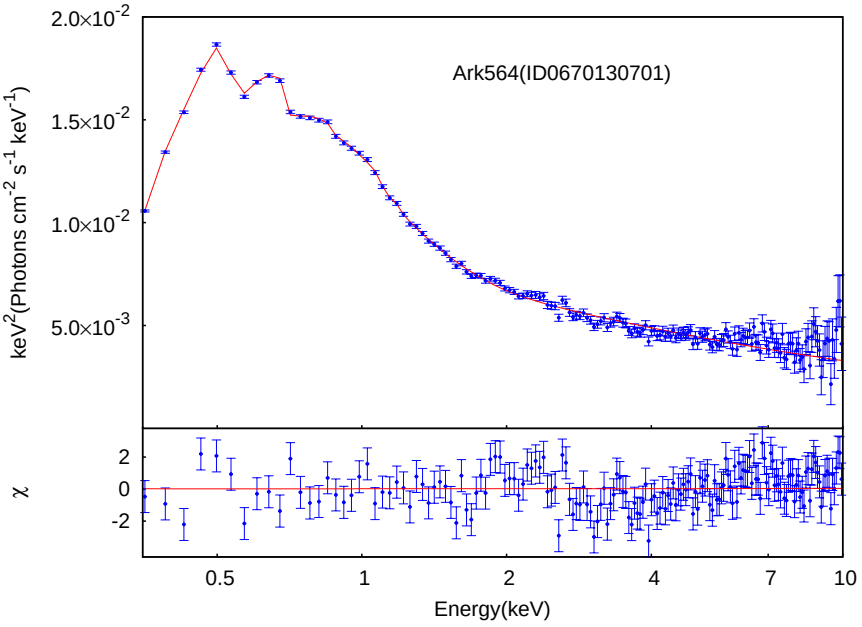

Figure 3.2: continued (ID067013061 & ID0510010701.)

fixed at 1000r_g. The inclination of the disk is fixed at 40°. For the "nthcomp" model we find that the results are not sensitive to the input seed photons which we fix to be a blackbody at 0.05 keV. For both the sources, addition of 2 or 3 low energy absorption edges improves the spectral fitting. The zedge model has three parameters, the energy of the edge (E_c), redshift, and optical depth (τ).

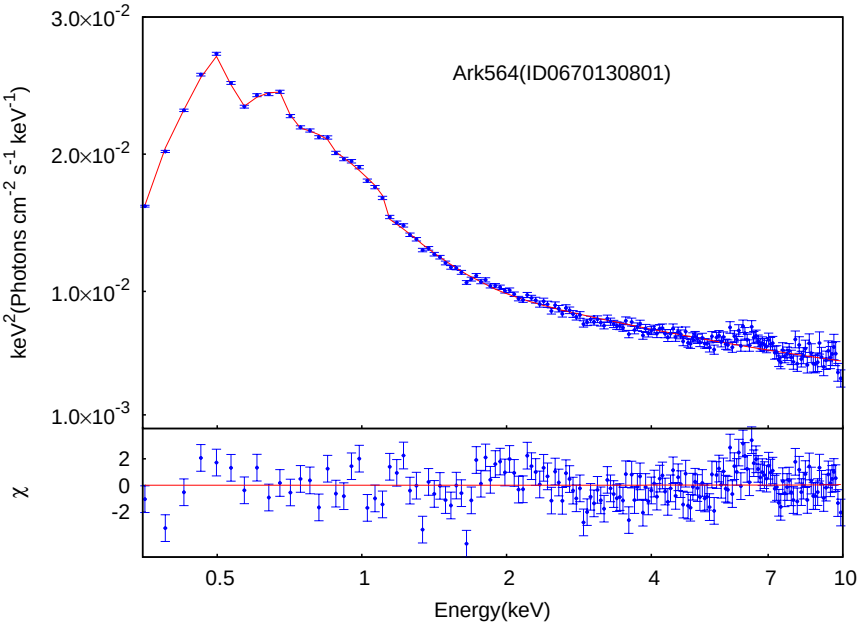

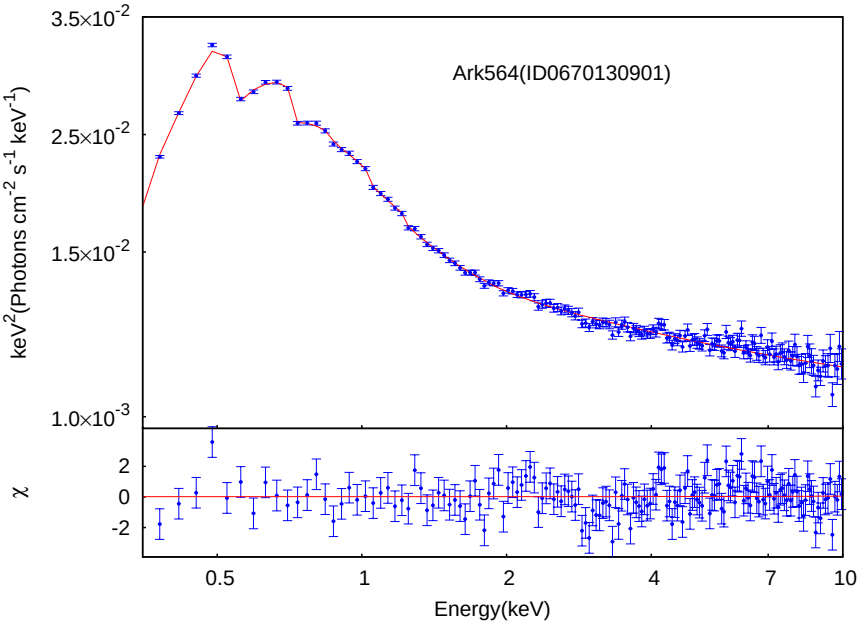

Figure 3.2: continued (ID0670130801 & ID0670130901)

We fixed the redshift to the source redshift. For one of the Mrk 335 observations (ID0306870101) there is also a hint of a narrow emission line at 7 keV. Figure 3.1 presents the unfolded spectra for the observations 0101040101, 0306870101, 0600540501, 0600540601 and 0510010701 of Mrk 335. The best fit spectral parameters for and the reduced χ^2 for all the observations of Mrk 335 and Ark 564

are listed in Tables 3.3, 3.4, 3.5 and 3.6.

The reduced χ^2 of the fits to the observations range from 1 to 1.6, which suggests that the underlying spectra may be more complex than the phenomenological model used here, especially at low energies. However for the motivation of this work, the phenomenological model used here is adequate since even for a reduced $\chi^2 \sim 1.6$, the model described the data well at a few percentage level and most of the discrepancies are at low energies. The high energy photon index is not too sensitive to the actual model used as we show later when we fit only the high energy part (3.0–10.0 keV) of the spectra and obtain qualitatively similar results. Nevertheless, we caution against over-interpretation of the best fit values obtained in these fits, especially for the components affecting the low energy part of the spectra.

3.6.1 The Effect of Complex Absorption and Reflection

The spectra of Mrk 335, may be affected by complex absorption and there may be a relativistically blurred reflection component which may dominate at low and high energies. Given the quality of the data many of these complex models may be degenerate, however in the present context it is useful to quantify the effect of these models on the high energy spectral index. The motivation here is not to obtain a physically self consistent model but rather to understand their effect of the high energy spectral index and hence in the primary result of this work.

To take into account the possibility of complex absorption, we include in the phenomenological model, partial ionised absorber represented by the XSPEC routine "zxipcf" [295]. The absorption is characterised by three parameters namely the column density, the covering fraction and the ionisation parameter of the absorber. For the addition of three parameters the changes in χ^2 for the four high flux observations with IDs 0101040101, 0306870101, 0600540601 and 0600540501 were 12.7, 22.0, 3.1, 9.0 and 12.0 respectively. More importantly, the best fit high energy spectral indexes obtained were 2.05 ± 0.05, 1.78 ± 0.06, 1.75 ± 0.05 and 1.81 ± 0.02. When compared with the high energy spectral indexes obtained from the phenomenological model, one can see that the errors are larger and any change in the index is less than 0.1. In contrast, for the deep low flux state, ID0510010701,

Table 3.3: Spectral parameters for Mrk 335 derived from different *XMM-Newton* observations in the (0.3–10.0)keV range.

Model	Parameter	0101040101	0306870101	0510010701
zedge1	E_c (keV)	0.63(froze)	$0.361^{+0.003}_{-0.004}$	$1.047^{+0.032}_{-0.035}$
	τ	$0.097^{+0.028}_{-0.031}$	$0.228^{+0.027}_{-0.006}$	$0.369^{+0.091}_{-0.093}$
zedge2	E_c (keV)	$1.127^{+0.042}_{-0.046}$	$1.120^{+0.034}_{-0.230}$	$1.509^{+0.060}_{-0.063}$
	τ	$0.063^{+0.031}_{-0.031}$	$0.026^{+0.006}_{-0.006}$	$0.377^{+0.101}_{-0.095}$
zedge3	E_c (keV)	-	-	0.686(Froze)
	τ	-	-	$0.524^{+0.104}_{-0.100}$
Diskline†	E_c (keV)	$6.313^{+0.362}_{-0.184}$	$6.275^{+0.032}_{-0.041}$	$6.009^{+0.056}_{-0.068}$
	β	$-2.609^{+0.749}_{-5.900}$	$-1.326^{+0.643}_{-0.414}$	$-9.668^{+3.607}_{-8.006}$
	Norm($\times 10^{-4}$)	$0.449^{+0.254}_{-0.168}$	$0.217^{+0.044}_{-0.038}$	$0.549^{+0.074}_{-0.076}$
zgaussian	E_c	-	$7.004^{+0.030}_{-0.031}$	-
	Norm($\times 10^{-3}$)	-	$0.007^{+0.002}_{-0.002}$	-
Simpl	Γ	$2.094^{+0.024}_{-0.049}$	$1.885^{+0.009}_{-0.005}$	$1.064^{+0.073}_{-0.046}$
	FracScat	$0.136^{+0.011}_{-0.009}$	$0.087^{+0.002}_{-0.001}$	$0.310^{+0.324}_{-0.104}$
nthComp	Γ	$2.862^{+0.052}_{-0.057}$	$3.277^{+0.008}_{-0.023}$	$1.980^{+0.094}_{-0.092}$
	kT(keV)	$0.266^{+0.051}_{-0.031}$	$0.823^{+0.019}_{-0.020}$	$0.210^{+0.019}_{-0.019}$
	Norm($\times 10^{-2}$)	$0.428^{+0.029}_{-0.032}$	$0.705^{+0.007}_{-0.037}$	$0.093^{+0.084}_{-0.039}$
Reduced χ^2/d.o.f.		1.04/144	1.48/163	1.70/130

†The values of r_{in} and r_{out} have been fixed at $6r_g$ and $1000r_g$ respectively while the inclination has been fixed at 40°.

the $\Delta\chi^2 = 45$ and the spectral index obtained was 1.55 ± 0.15 which is significantly different from the phenomenological model.

Next we consider the possible effect of a complex relativistically blurred reflection component in the spectra. Since, the ionised reflection component produces a complex soft excess which needs to be modelled with absorption, we limit our analysis to energies > 2 keV. This is adequate since our interest here is to study the effect of the component on the high energy index. Since for the phenomenological model, the spectra shows the presence of a narrow and broad Iron lines, we consider a power-law and two reflection components represented by the table model "reflionx" [296]. For one of the the reflection component we convolve it us-

Table 3.4: Spectral parameters for Mrk 335 derived from different *XMM-Newton* observations in the (0.3–10.0)keV range.

Model	Parameter	0600540601	0600540501
zedge1	E_c (keV)	$0.730^{+0.004}_{-0.003}$	$0.730^{+0.004}_{-0.004}$
	τ	$0.776^{+0.027}_{-0.042}$	$0.553^{+0.029}_{-0.017}$
zedge2	E_c (keV)	$0.943^{+0.011}_{-0.012}$	$0.922^{+0.014}_{-0.011}$
	τ	$0.313^{+0.030}_{-0.041}$	$0.238^{+0.024}_{-0.040}$
zedge3	E_c (keV)	-	-
	τ	-	-
Diskline†	E_c (keV)	$6.022^{+0.050}_{-0.061}$	$5.952^{+0.070}_{-0.064}$
	β	$-7.416^{+2.297}_{-4.753}$	$-5.061^{+1.497}_{-4.475}$
	Norm($\times 10^{-4}$)	$0.276^{+0.034}_{-0.033}$	$0.292^{+0.042}_{-0.022}$
zgaussian	E_c	-	-
	Norm($\times 10^{-3}$)	-	-
Simpl	Γ	$1.676^{+0.018}_{-0.007}$	$1.787^{+0.018}_{-0.008}$
	FracScat	$0.233^{+0.012}_{-0.007}$	$0.193^{+0.007}_{-0.005}$
nthComp	Γ	$1.922^{+0.087}_{-0.213}$	$2.043^{+0.069}_{-0.219}$
	kT(keV)	$0.153^{+0.008}_{-0.018}$	$0.159^{+0.008}_{-0.020}$
	Norm($\times 10^{-2}$)	$0.060^{+0.003}_{-0.008}$	$0.091^{+0.006}_{-0.009}$
Reduced χ^2/d.o.f.		1.40/161	1.52/159

†The values of r_{in} and r_{out} have been fixed at $6r_g$ and $1000r_g$ respectively while the inclination has been fixed at 40°.

ing the relativistic blurring model "kdblur" where we fix the inner and outer radii, but allow for the emissivity index to be free. The best fit power-law index for the four high flux state observations with IDs 0101040101, 0306870101, 0600540601 and 0600540501 were 2.09 ± 0.05, 2.16 ± 0.02, 1.77 ± 0.03 and 1.64 ± 0.05. We note that for the observation with ID. 0306870101 the change in spectral index as compared to the phenomenological model is ~ 0.28 while for the others it is

Table 3.5: Spectral parameters for Ark 564 derived from different *XMM-Newton* observations in the (0.3–10.0)keV range.

Model	Parameter	0006810101	0670130301	0670130801
zedge1	E_c (keV)	$0.508^{+0.013}_{-0.015}$	$0.708^{+0.008}_{-0.008}$	$0.345^{+0.013}_{-0.015}$
	τ	$0.111^{+0.022}_{-0.022}$	$0.105^{+0.012}_{-0.010}$	$0.244^{+0.050}_{-0.051}$
zedge2	E_c (keV)	$0.712^{+0.011}_{-0.013}$	$1.054^{+0.041}_{-0.045}$	$0.713^{+0.012}_{-0.006}$
	τ	$0.147^{+0.030}_{-0.022}$	$0.033^{+0.013}_{-0.014}$	$0.072^{+0.013}_{-0.010}$
zedge3	E_c (keV)	$1.122^{+0.126}_{-0.094}$	$1.231^{+0.038}_{-0.039}$	$1.160^{+0.019}_{-0.018}$
	τ	$0.022^{+0.023}_{-0.022}$	$0.047^{+0.015}_{-0.014}$	$0.086^{+0.013}_{-0.007}$
Simpl	Γ	$2.474^{+0.024}_{-0.023}$	$2.513^{+0.014}_{-0.013}$	$2.418^{+0.014}_{-0.008}$
	FracScat	$0.193^{+0.008}_{-0.007}$	$0.192^{+0.004}_{-0.005}$	$0.153^{+0.004}_{-0.004}$
nthComp	Γ	$2.295^{+0.052}_{-0.047}$	$2.292^{+0.010}_{-0.019}$	$2.676^{+0.059}_{-0.050}$
	kT(keV)	$0.184^{+0.020}_{-0.020}$	$0.195^{+0.009}_{-0.008}$	$0.220^{+0.027}_{-0.020}$
	Norm	$0.014^{+0.0008}_{-0.0009}$	$0.012^{+0.0003}_{-0.0003}$	$0.011^{+0.0004}_{-0.0003}$
Reduced χ^2/d.o.f.		1.03/149	1.58/161	1.62/160
Model	Parameter	0670130901	0670130201	0670130601
zedge1	E_c (keV)	$0.723^{+0.010}_{-0.010}$	$0.330^{+0.011}_{-0.018}$	$0.347^{+0.005}_{-0.006}$
	τ	$0.093^{+0.014}_{-0.013}$	$0.359^{+0.274}_{-0.044}$	$0.269^{+0.044}_{-0.021}$
zedge2	E_c (keV)	$1.071^{+0.053}_{-0.062}$	$0.751^{+0.020}_{-0.023}$	$0.714^{+0.011}_{-0.012}$
	τ	$0.029^{+0.019}_{-0.011}$	$0.045^{+0.013}_{-0.007}$	$0.063^{+0.012}_{-0.012}$
zedge3	E_c (keV)	$1.231^{+0.159}_{-0.087}$	$1.217^{+0.033}_{-0.031}$	$1.127^{+0.021}_{-0.019}$
	τ	$0.023^{+0.020}_{-0.018}$	$0.057^{+0.014}_{-0.014}$	$0.072^{+0.011}_{-0.011}$
Simpl	Γ	$2.495^{+0.018}_{-0.017}$	$2.448^{+0.019}_{-0.009}$	$2.428^{+0.015}_{-0.014}$
	FracScat	$0.194^{+0.006}_{-0.006}$	$0.152^{+0.005}_{-0.005}$	$0.151^{+0.004}_{-0.004}$
nthComp	Γ	$2.353^{+0.016}_{-0.022}$	$2.795^{+0.063}_{-0.055}$	$2.862^{+0.051}_{-0.044}$
	kT(keV)	$0.192^{+0.011}_{-0.010}$	$0.240^{+0.032}_{-0.023}$	$0.254^{+0.031}_{-0.022}$
	Norm	$0.013^{+0.0004}_{-0.0003}$	$0.015^{+0.0005}_{-0.0004}$	$0.011^{+0.0004}_{-0.0003}$
Reduced χ^2/d.o.f.		1.17/158	1.03/159	1.30/164

Table 3.6: Spectral parameters for Ark 564 derived from different *XMM-Newton* observations in the (0.3–10.0)keV range.

Model	Parameter	0670130501	0006810301	0206400101
zedge1	E_c (keV)	$0.346^{+0.006}_{-0.007}$	$0.338^{+0.006}_{-0.007}$	$0.513^{+0.006}_{-0.006}$
	τ	$0.406^{+0.039}_{-0.044}$	$0.595^{+0.226}_{-0.226}$	$0.093^{+0.008}_{-0.009}$
zedge2	E_c (keV)	$0.718^{+0.012}_{-0.009}$	$0.489^{+0.012}_{-0.012}$	$0.706^{+0.005}_{-0.007}$
	τ	$0.069^{+0.011}_{-0.011}$	$0.188^{+0.024}_{-0.017}$	$0.116^{+0.011}_{-0.012}$
zedge3	E_c (keV)	$1.197^{+0.023}_{-0.020}$	$0.710^{+0.015}_{-0.017}$	$1.111^{+0.018}_{-0.019}$
	τ	$0.068^{+0.012}_{-0.012}$	$0.102^{+0.017}_{-0.016}$	$0.054^{+0.009}_{-0.009}$
Simpl	Γ	$2.437^{+0.011}_{-0.014}$	$2.376^{+0.009}_{-0.012}$	$2.472^{+0.009}_{-0.004}$
	FracScat	$0.144^{+0.004}_{-0.004}$	$0.085^{+0.015}_{-0.015}$	$0.183^{+0.003}_{-0.003}$
nthComp	Γ	$2.892^{+0.029}_{-0.029}$	$3.127^{+0.024}_{-0.021}$	$2.381^{+0.019}_{-0.022}$
	kT(keV)	$0.250^{+0.032}_{-0.023}$	$0.240^{+0.006}_{-0.004}$	$0.188^{+0.009}_{-0.008}$
	Norm	$0.012^{+0.0004}_{-0.0002}$	$0.009^{+0.00003}_{-0.0001}$	$0.010^{+0.0001}_{-0.0003}$
Reduced χ^2/d.o.f.		1.35/163	1.16/148	1.62/165
Model	Parameter	0670130701	0670130401	
zedge1	E_c (keV)	$0.587^{+0.045}_{-0.037}$	$0.341^{+0.008}_{-0.018}$	
	τ	$0.035^{+0.019}_{-0.020}$	$0.303^{+0.041}_{-0.041}$	
zedge2	E_c (keV)	$0.716^{+0.013}_{-0.011}$	$0.710^{+0.009}_{-0.005}$	
	τ	$0.126^{+0.017}_{-0.024}$	$0.075^{+0.012}_{-0.012}$	
zedge3	E_c (keV)	$1.143^{+0.023}_{-0.027}$	$1.164^{+0.030}_{-0.032}$	
	τ	$0.061^{+0.014}_{-0.014}$	$0.046^{+0.011}_{-0.011}$	
Simpl	Γ	$2.436^{+0.016}_{-0.016}$	$2.416^{+0.012}_{-0.015}$	
	FracScat	$0.183^{+0.004}_{-0.005}$	$0.159^{+0.005}_{-0.004}$	
nthComp	Γ	$2.175^{+0.022}_{-0.027}$	$2.748^{+0.049}_{-0.051}$	
	kT(keV)	$0.191^{+0.009}_{-0.008}$	$0.233^{+0.032}_{-0.022}$	
	Norm	$0.009^{+0.0002}_{-0.0003}$	$0.011^{+0.0003}_{-0.0003}$	
Reduced χ^2/d.o.f.		1.51/163	1.49/164	

< 0.15. For the deep low flux state, ID0510010701, the spectral index obtained was $3.00 \pm .07$ which is radically different than the value obtained earlier.

Thus, the effect of complex absorption or reflection is dramatic for the deep low state. This is expected based on the analysis of Grupe et al. [297]. For the other higher flux states, complex absorption may change the index by < 0.1 from those of the phenomenological model. The effect of complex reflection on the index is also modest < 0.15 but we note that it may be large ~ 0.28 for the observation with ID0306870101, which incidentally is also the highest flux state in the sample.

3.7 Flux Resolved Spectroscopy

A light curve is defined as a graph which shows the brightness of an object over a period of time. The study of light curve help us to understand processes at work within the object. The light curves for each of the observations of Mrk 335 and Ark 564 are shown in Figure 3.3 & 3.4 which reveals that for nearly all observations there is significant flux variation in timescales of $\sim 10^4$ s.

To investigate the variation of the photon index, each observation was split into 3 or 4 flux levels (marked by horizontal dotted lines in Figures 3.3 & 3.4) and the corresponding spectrum was generated. During the 2007 observation of Mrk 335 (ID0510010701), the count rate was too low for the data to be split into different flux levels.

Each of the flux level spectra was fitted with the same model used for the average spectra. However, due to the lower statistics of the flux resolved spectra, there were several parameters which were either not constrained or were consistent within error bars to be not varying during the observations. Thus, several spectral parameters were fixed to their best fit values obtained from the fitting of the average spectra. These were, the energies of the different edges and emission lines, the temperature and normalisation of the soft photon Comptonization (i.e. kT_{bb} and normalisation of the "nthcomp" component) and the normalisation and emissivity index of the Iron line (i.e. β and normalisation of the "diskline" component). The results of the flux resolved spectroscopy are presented in Table 3.7.

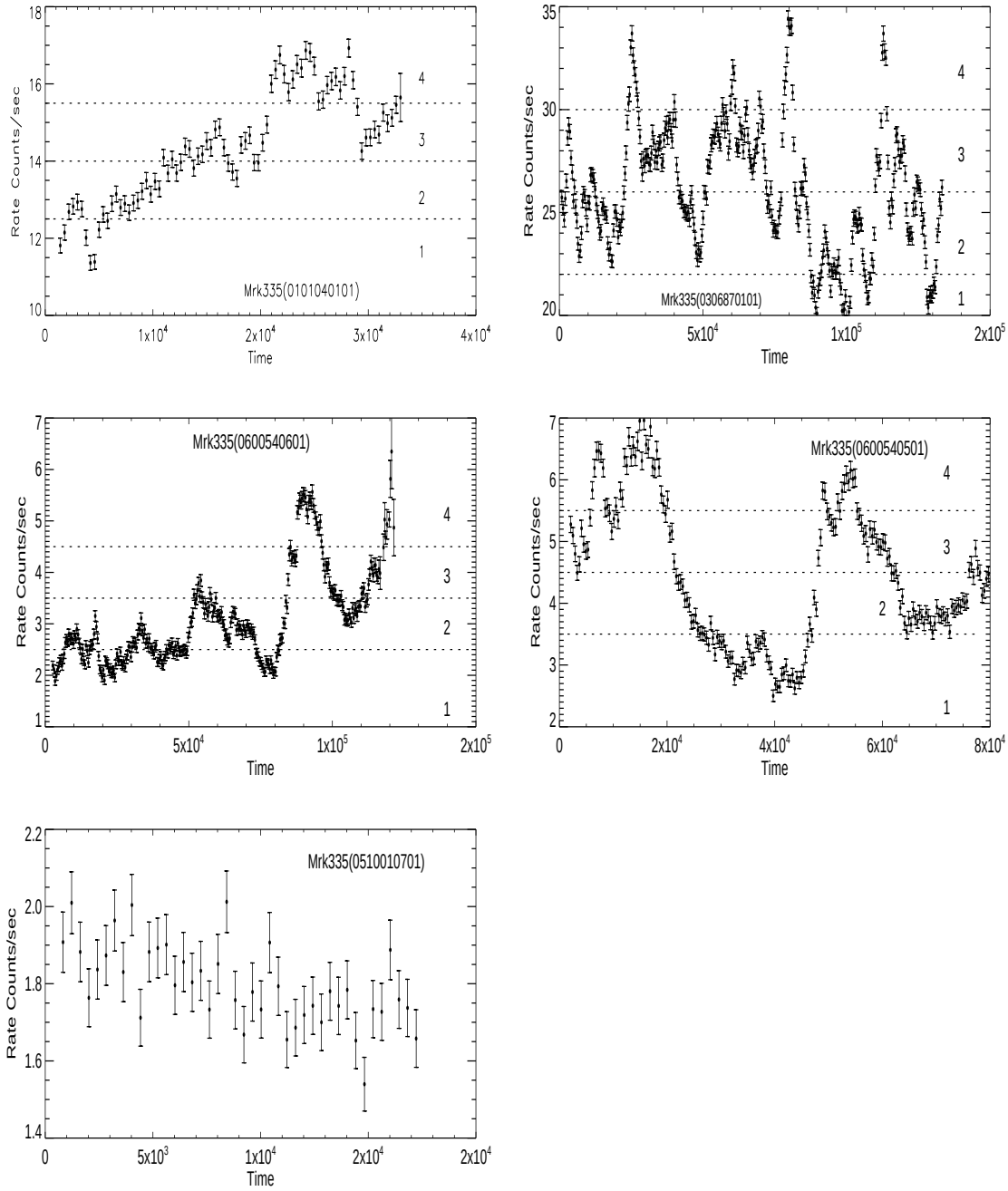

Figure 3.3: EPIC PN light curve (in 400 s bins) of Mrk 335. The light curves were extracted in the energy range of (0.3–10.0) keV. The time ranges for flux resolved spectroscopy have been selected corresponding to different counts s^{-1} as shown by the horizontal dotted lines.

3.7.1 Eddington Ratio

For each flux resolved spectra, the unabsorbed flux in the 0.3–10.0 keV band was computed using the XSPEC model "cflux". The fluxes were converted into

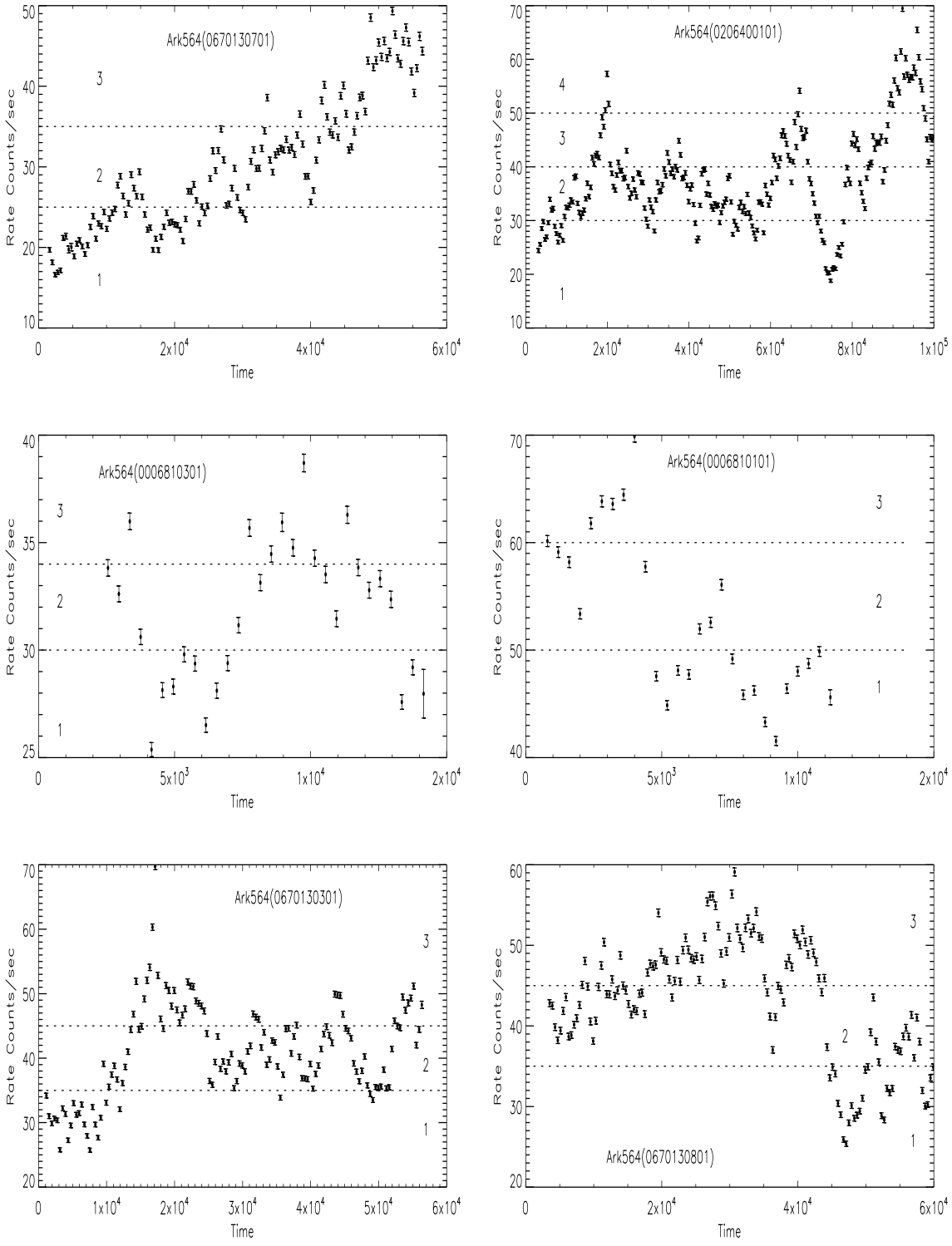

Figure 3.4: EPIC PN light curve (in 400 s bins) of Ark 564. The light curves were extracted in the energy range of (0.3–10.0) keV. The time ranges for flux resolved spectroscopy have been selected corresponding to different counts s^{-1} as shown by the horizontal dotted lines.

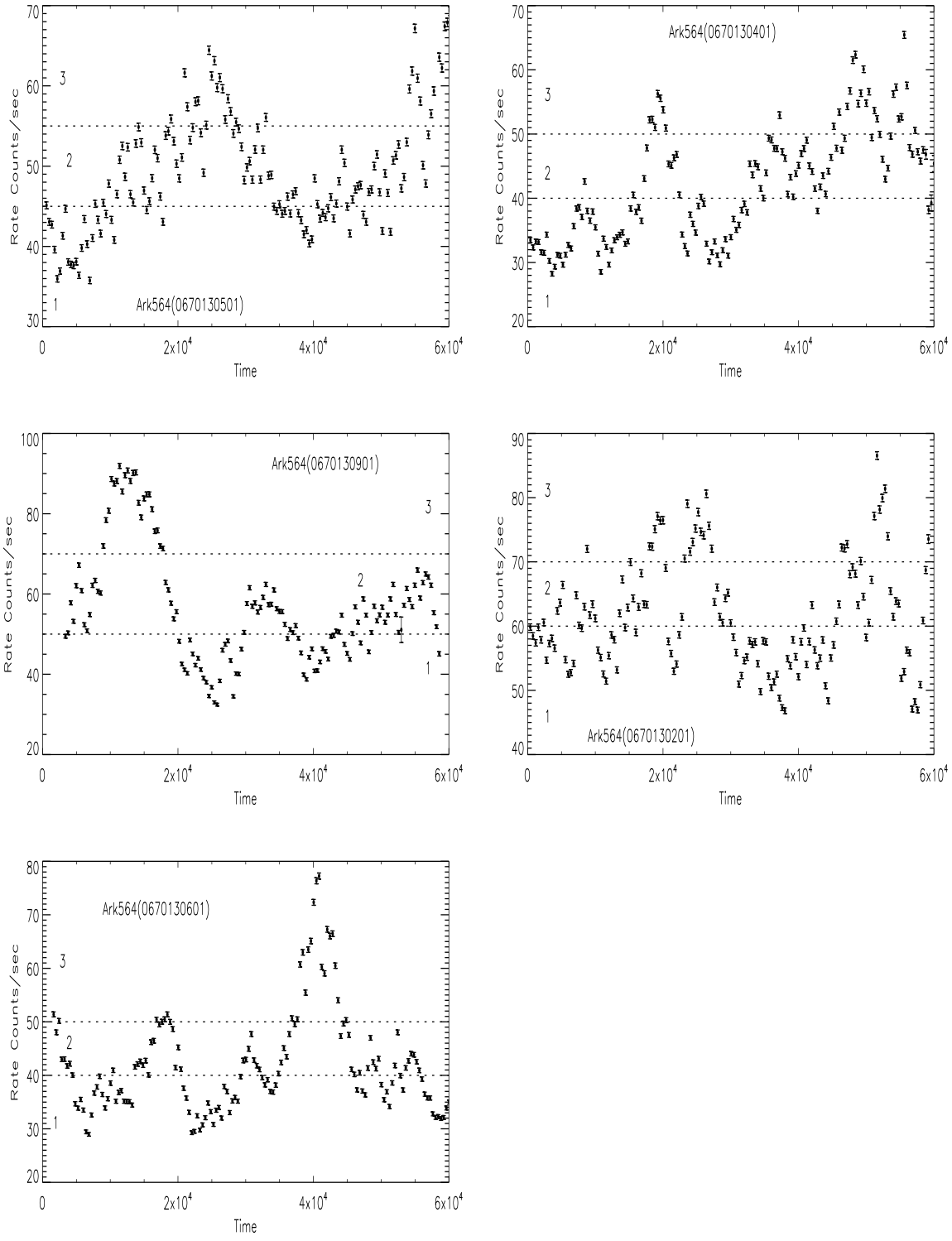

Figure 3.4: continued

luminosities, L by using the luminosity distances of 103 Mpc for Mrk 335 and 98.5 Mpc for Ark 564, which are the average values quoted in the NED website.

Table 3.7: Spectral parameters for each flux state (for Mrk 335 & Ark 564) derived from different *XMM-Newton* observations in the (0.3-10.0)keV range.

obs ID	flux state	zedge1	zedge2	zedge3	Simpl		nthComp	red χ^2/d.o.f.
		τ	τ	τ	Γ	FracScat	Γ	
0101040101	1	$0.002\times10^{-4+908.7}_{-0.002}$	$0.073^{+0.101}_{-0.065}$	-	$2.114^{+0.157}_{-0.151}$	$0.140^{+0.039}_{-0.030}$	$2.979^{+0.125}_{-0.190}$	0.92/ 82
(Mrk 335)	2	$0.132^{+0.055}_{-0.055}$	$0.024^{+0.055}_{-0.024}$	-	$2.017^{+0.078}_{-0.076}$	$0.120^{+0.016}_{-0.013}$	$2.780^{+0.096}_{-0.084}$	1.01/120
	3	$0.098^{+0.055}_{-0.055}$	$0.074^{+0.053}_{-0.053}$	-	$2.145^{+0.080}_{-0.077}$	$0.140^{+0.020}_{-0.017}$	$2.921^{+0.127}_{-0.106}$	0.89/120
	4	$0.077^{+0.063}_{-0.063}$	$0.070^{+0.061}_{-0.061}$	-	$2.177^{+0.093}_{-0.090}$	$0.160^{+0.028}_{-0.022}$	$2.896^{+0.162}_{-0.127}$	1.05/112
0306870101	1	$0.250^{+0.167}_{-0.156}$	$0.045^{+0.034}_{-0.034}$	-	$1.943^{+0.072}_{-0.084}$	$0.102^{+0.013}_{-0.012}$	$3.373^{+0.212}_{-0.197}$	1.09/152
(Mrk 335)	2	$0.209^{+0.053}_{-0.052}$	$0.019^{+0.014}_{-0.014}$	-	$1.854^{+0.032}_{-0.034}$	$0.083^{+0.004}_{-0.004}$	$3.255^{+0.061}_{-0.060}$	1.21/169
	3	$0.262^{+0.061}_{-0.059}$	$0.022^{+0.014}_{-0.014}$	-	$1.917^{+0.033}_{-0.035}$	$0.087^{+0.005}_{-0.004}$	$3.319^{+0.074}_{-0.071}$	1.17/169
	4	$0.342^{+0.099}_{-0.098}$	$0.028^{+0.024}_{-0.024}$	-	$1.952^{+0.047}_{-0.051}$	$0.099^{+0.009}_{-0.008}$	$3.399^{+0.117}_{-0.116}$	1.10/159
0600540601	1	$0.638^{+0.060}_{-0.059}$	$0.268^{+0.054}_{-0.053}$	-	$1.622^{+0.035}_{-0.034}$	$0.225^{+0.012}_{-0.011}$	$2.009^{+0.088}_{-0.084}$	1.30/152
(Mrk 335)	2	$0.776^{+0.043}_{-0.043}$	$0.276^{+0.039}_{-0.038}$	-	$1.653^{+0.025}_{-0.024}$	$0.243^{+0.009}_{-0.009}$	$1.918^{+0.063}_{-0.061}$	1.31/160
	3	$0.877^{+0.068}_{-0.067}$	$0.387^{+0.063}_{-0.062}$	-	$1.768^{+0.042}_{-0.041}$	$0.246^{+0.014}_{-0.013}$	$1.860^{+0.090}_{-0.085}$	1.13/145
	4	$0.862^{+0.075}_{-0.074}$	$0.435^{+0.072}_{-0.071}$	-	$1.802^{+0.048}_{-0.047}$	$0.216^{+0.015}_{-0.014}$	$1.936^{+0.099}_{-0.094}$	1.29/137
0600540501	1	$0.598^{+0.070}_{-0.069}$	$0.087^{+0.059}_{-0.059}$	-	$1.711^{+0.047}_{-0.046}$	$0.179^{+0.011}_{-0.011}$	$1.995^{+0.094}_{-0.090}$	1.29/140
(Mrk 335)	2	$0.605^{+0.052}_{-0.052}$	$0.273^{+0.047}_{-0.046}$	-	$1.755^{+0.034}_{-0.033}$	$0.192^{+0.009}_{-0.009}$	$2.012^{+0.071}_{-0.069}$	1.12/153
	3	$0.530^{+0.052}_{-0.052}$	$0.229^{+0.047}_{-0.047}$	-	$1.805^{+0.036}_{-0.035}$	$0.191^{+0.010}_{-0.009}$	$2.109^{+0.073}_{-0.070}$	1.24/150
	4	$0.513^{+0.048}_{-0.048}$	$0.294^{+0.045}_{-0.044}$	-	$1.891^{+0.034}_{-0.034}$	$0.209^{+0.010}_{-0.010}$	$2.071^{+0.069}_{-0.067}$	1.29/147
0006810101	1	$0.107^{+0.041}_{-0.041}$	$0.121^{+0.046}_{-0.046}$	$-0.006^{+0.037}_{-0.036}$	$2.473^{+0.037}_{-0.036}$	$0.189^{+0.013}_{-0.012}$	$2.401^{+0.085}_{-0.076}$	0.93/137
(Akn 564)	2	$0.093^{+0.048}_{-0.048}$	$0.127^{+0.054}_{-0.054}$	$0.041^{+0.044}_{-0.044}$	$2.496^{+0.045}_{-0.044}$	$0.197^{+0.017}_{-0.015}$	$2.289^{+0.093}_{-0.083}$	0.99/130
	3	$0.124^{+0.051}_{-0.052}$	$0.199^{+0.059}_{-0.059}$	$0.045^{+0.047}_{-0.047}$	$2.491^{+0.048}_{-0.047}$	$0.204^{+0.018}_{-0.016}$	$2.177^{+0.092}_{-0.082}$	1.05/126
0670130301	1	$0.126^{+0.031}_{-0.030}$	$0.033^{+0.027}_{-0.027}$	$0.051^{+0.031}_{-0.031}$	$2.456^{+0.036}_{-0.036}$	$0.173^{+0.011}_{-0.010}$	$2.329^{+0.047}_{-0.045}$	1.28/148
(Akn 564)	2	$0.108^{+0.018}_{-0.020}$	$0.039^{+0.016}_{-0.016}$	$0.064^{+0.018}_{-0.018}$	$2.530^{+0.022}_{-0.021}$	$0.194^{+0.007}_{-0.007}$	$2.305^{+0.029}_{-0.028}$	1.20/159
	3	$0.102^{+0.020}_{-0.020}$	$0.034^{+0.018}_{-0.018}$	$0.030^{+0.020}_{-0.020}$	$2.536^{+0.024}_{-0.024}$	$0.202^{+0.008}_{-0.008}$	$2.246^{+0.031}_{-0.030}$	1.42/157
0670130801	1	$0.082^{+0.148}_{-0.082}$	$0.088^{+0.038}_{-0.038}$	$0.089^{+0.038}_{-0.038}$	$2.355^{+0.041}_{-0.041}$	$0.163^{+0.014}_{-0.013}$	$2.633^{+0.138}_{-0.094}$	0.98/139
(Akn 564)	2	$0.218^{+0.083}_{-0.081}$	$0.080^{+0.021}_{-0.021}$	$0.091^{+0.022}_{-0.022}$	$2.383^{+0.024}_{-0.024}$	$0.146^{+0.007}_{-0.007}$	$2.636^{+0.071}_{-0.067}$	1.35/157
	3	$0.285^{+0.072}_{-0.070}$	$0.065^{+0.018}_{-0.018}$	$0.084^{+0.019}_{-0.019}$	$2.475^{+0.022}_{-0.021}$	$0.160^{+0.007}_{-0.007}$	$2.709^{+0.065}_{-0.062}$	1.38/159
0670130901	1	$0.017^{+0.028}_{-0.028}$	$0.070^{+0.030}_{-0.030}$	$0.024^{+0.032}_{-0.032}$	$2.434^{+0.035}_{-0.034}$	$0.179^{+0.011}_{-0.010}$	$2.383^{+0.048}_{-0.046}$	1.22/145
(Akn 564)	2	$0.049^{+0.021}_{-0.021}$	$0.100^{+0.022}_{-0.022}$	$0.031^{+0.024}_{-0.023}$	$2.531^{+0.027}_{-0.027}$	$0.184^{+0.009}_{-0.008}$	$2.386^{+0.036}_{-0.035}$	1.11/152
	3	$0.013^{+0.028}_{-0.028}$	$0.095^{+0.031}_{-0.031}$	$-0.003^{+0.031}_{-0.031}$	$2.519^{+0.035}_{-0.034}$	$0.241^{+0.016}_{-0.014}$	$2.261^{+0.053}_{-0.050}$	1.08/143
0670130201	1	$0.338^{+0.081}_{-0.079}$	$0.042^{+0.021}_{-0.021}$	$0.049^{+0.022}_{-0.022}$	$2.437^{+0.028}_{-0.027}$	$0.142^{+0.007}_{-0.007}$	$2.806^{+0.073}_{-0.069}$	0.80/158
(Akn 564)	2	$0.314^{+0.104}_{-0.101}$	$0.052^{+0.026}_{-0.026}$	$0.085^{+0.027}_{-0.027}$	$2.471^{+0.034}_{-0.034}$	$0.167^{+0.011}_{-0.010}$	$2.770^{+0.099}_{-0.090}$	1.02/150
	3	$0.506^{+0.123}_{-0.117}$	$0.040^{+0.029}_{-0.029}$	$0.044^{+0.029}_{-0.029}$	$2.483^{+0.037}_{-0.037}$	$0.161^{+0.012}_{-0.011}$	$2.858^{+0.118}_{-0.106}$	0.95/148
0670130601	1	$0.218^{+0.069}_{-0.067}$	$0.083^{+0.018}_{-0.018}$	$0.090^{+0.019}_{-0.019}$	$2.372^{+0.023}_{-0.022}$	$0.145^{+0.006}_{-0.006}$	$2.793^{+0.066}_{-0.062}$	1.05/164
(Akn 564)	2	$0.216^{+0.077}_{-0.075}$	$0.048^{+0.020}_{-0.020}$	$0.082^{+0.021}_{-0.021}$	$2.452^{+0.025}_{-0.024}$	$0.157^{+0.008}_{-0.007}$	$2.867^{+0.079}_{-0.074}$	1.19/160
	3	$0.466^{+0.103}_{-0.100}$	$0.061^{+0.024}_{-0.024}$	$0.033^{+0.025}_{-0.025}$	$2.537^{+0.030}_{-0.030}$	$0.163^{+0.011}_{-0.010}$	$3.014^{+0.110}_{-0.102}$	1.05/151
0670130501	1	$0.090^{+0.025}_{-0.025}$	$0.092^{+0.023}_{-0.023}$	$0.368^{+0.086}_{-0.084}$	$2.382^{+0.032}_{-0.032}$	$0.122^{+0.007}_{-0.007}$	$2.854^{+0.077}_{-0.072}$	1.05/154
(Akn 564)	2	$0.069^{+0.017}_{-0.017}$	$0.063^{+0.016}_{-0.016}$	$0.393^{+0.066}_{-0.064}$	$2.456^{+0.022}_{-0.022}$	$0.151^{+0.007}_{-0.006}$	$2.920^{+0.066}_{-0.062}$	1.18/161
	3	$0.046^{+0.023}_{-0.023}$	$0.052^{+0.022}_{-0.022}$	$0.491^{+0.092}_{-0.089}$	$2.485^{+0.030}_{-0.030}$	$0.158^{+0.010}_{-0.009}$	$2.930^{+0.092}_{-0.085}$	1.20/153
0006810301	1	$0.092^{+0.509}_{-0.493}$	$0.055^{+0.145}_{-0.147}$	$-0.005^{+0.071}_{-0.071}$	$2.390^{+0.079}_{-0.079}$	$0.103^{+0.030}_{-0.024}$	$3.023^{+0.302}_{-0.280}$	1.03/118
(Akn 564)	2	$1.112^{+0.428}_{-0.440}$	$0.335^{+0.118}_{-0.124}$	$0.158^{+0.061}_{-0.061}$	$2.407^{+0.063}_{-0.064}$	$0.065^{+0.016}_{-0.012}$	$3.386^{+0.242}_{-0.240}$	0.95/127
	3	$1.297^{+0.551}_{-0.542}$	$0.365^{+0.145}_{-0.148}$	$0.187^{+0.069}_{-0.069}$	$2.479^{+0.069}_{-0.069}$	$0.076^{+0.024}_{-0.018}$	$3.455^{+0.324}_{-0.306}$	1.18/124
0206400101	1	$0.131^{+0.029}_{-0.029}$	$0.128^{+0.033}_{-0.033}$	$0.061^{+0.028}_{-0.028}$	$2.409^{+0.028}_{-0.028}$	$0.164^{+0.008}_{-0.008}$	$2.387^{+0.055}_{-0.052}$	1.11/154
(Akn 564)	2	$0.107^{+0.015}_{-0.015}$	$0.121^{+0.017}_{-0.017}$	$0.054^{+0.014}_{-0.014}$	$2.443^{+0.014}_{-0.014}$	$0.177^{+0.004}_{-0.004}$	$2.381^{+0.030}_{-0.029}$	1.16/163
	3	$0.071^{+0.019}_{-0.019}$	$0.105^{+0.022}_{-0.022}$	$0.054^{+0.018}_{-0.018}$	$2.527^{+0.018}_{-0.018}$	$0.190^{+0.006}_{-0.006}$	$2.414^{+0.039}_{-0.037}$	1.24/160
	4	$0.059^{+0.023}_{-0.024}$	$0.109^{+0.027}_{-0.027}$	$0.055^{+0.022}_{-0.022}$	$2.533^{+0.022}_{-0.022}$	$0.213^{+0.009}_{-0.008}$	$2.352^{+0.050}_{-0.047}$	1.02/155
0670130701	1	$0.094^{+0.029}_{-0.029}$	$0.150^{+0.029}_{-0.029}$	$0.057^{+0.025}_{-0.025}$	$2.412^{+0.032}_{-0.031}$	$0.172^{+0.009}_{-0.008}$	$2.195^{+0.047}_{-0.044}$	1.19/148
(Akn 564)	2	$0.076^{+0.022}_{-0.022}$	$0.133^{+0.022}_{-0.022}$	$0.043^{+0.019}_{-0.019}$	$2.443^{+0.025}_{-0.024}$	$0.186^{+0.008}_{-0.007}$	$2.187^{+0.036}_{-0.034}$	1.17/155
	3	$0.025^{+0.024}_{-0.024}$	$0.106^{+0.024}_{-0.024}$	$0.009^{+0.020}_{-0.009}$	$2.468^{+0.032}_{-0.032}$	$0.191^{+0.010}_{-0.009}$	$2.157^{+0.039}_{-0.038}$	1.23/160
0670130401	1	$0.217^{+0.074}_{-0.072}$	$0.079^{+0.019}_{-0.019}$	$0.054^{+0.020}_{-0.019}$	$2.386^{+0.023}_{-0.023}$	$0.156^{+0.007}_{-0.007}$	$2.739^{+0.068}_{-0.064}$	1.30/161
(Akn 564)	2	$0.317^{+0.073}_{-0.072}$	$0.077^{+0.019}_{-0.019}$	$0.044^{+0.019}_{-0.019}$	$2.406^{+0.024}_{-0.024}$	$0.156^{+0.007}_{-0.007}$	$2.731^{+0.067}_{-0.063}$	1.14/164
	3	$0.450^{+0.091}_{-0.088}$	$0.073^{+0.022}_{-0.022}$	$0.038^{+0.022}_{-0.022}$	$2.491^{+0.028}_{-0.028}$	$0.171^{+0.010}_{-0.009}$	$2.814^{+0.087}_{-0.081}$	1.18/159

For Mrk 335, the black hole mass was taken to be 1.4 $\times 10^7$ $M_\odot$ [242, 243] while for Ark 564 we adopt a value of 2.61 $\times$ 10^6 $M_\odot$ [233] to obtain their respective Eddington luminosities L_{Edd}. We have measured X-ray Eddington ratio which is λ_{Edd}=L_x/L_{Edd}, L_x being the X-ray luminosity for all flux levels of both the sources.

3.8 Results

In Figure 3.5, the high energy photon index is plotted against the X-ray Eddington ratio for the different flux resolved spectra for MRK 335. Three of the observations cover an order of magnitude range in X-ray Eddington ratio from 0.004 to 0.04 and show a tight correlation between the photon index and X-ray Eddington ratio. A straight line fit to these three observation sets gives a slope $m = 0.64 \pm 0.04$,

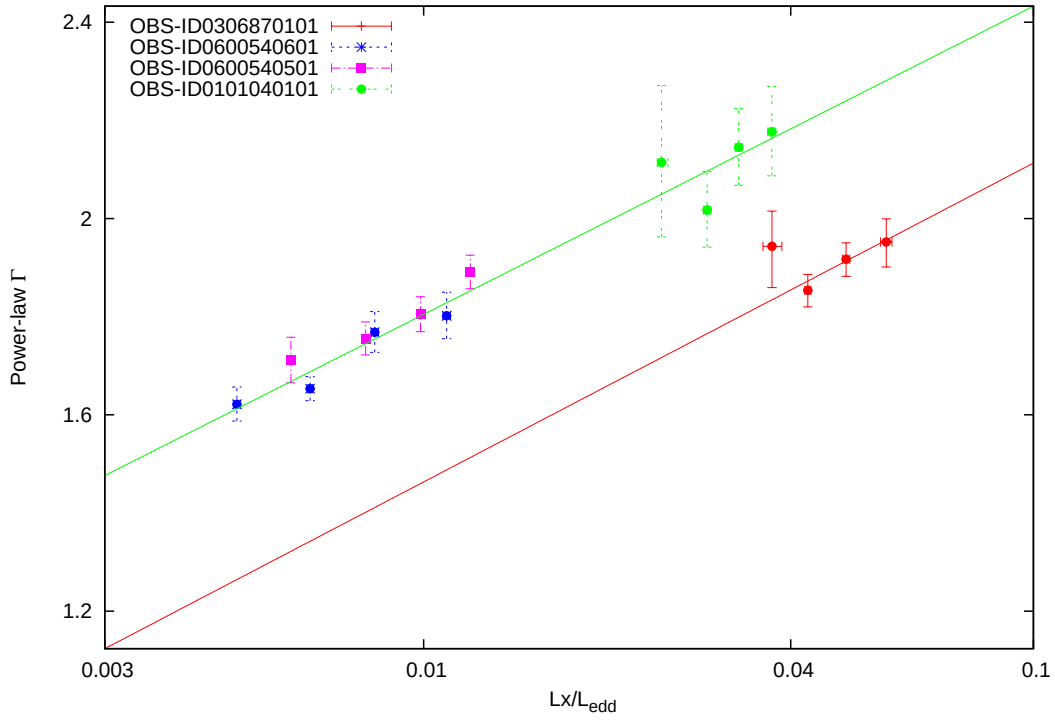

Figure 3.5: The high energy photon index, Γ versus the X-ray Eddington ratio for Mrk 335. The X-ray Eddington ratio is L_X/L_{Edd} where L_X is the unabsorbed luminosity in the 0.3–10.0 keV range.

intercept $c = 3.08 \pm 0.08$ and reduced $\chi^2 = 0.57$. The observation with the highest X-ray Eddington ratio > 0.04, does not follow the linear relation. Instead

fitting the flux resolved spectra for that observation only, one gets a straight line with slope $m = 0.65 \pm 0.04$, intercept $c = 2.76 \pm 0.07$ and reduced $\chi^2 = 0.76$. In other words, the data follows a parallel track. Note that the lowest luminosity observation ($L_X/L_{Edd} \sim 0.002$) was not included in the straight line fit. Nevertheless, the fit to the high flux data, passes through the lowest flux one.

To verify that the results do not depend sensitively on the phenomenological spectral model used, we repeat the flux resolved spectroscopy analysis using only the energy band 3.0–10.0 keV. We fit this energy band with a power-law and a broad Iron line. Figure 3.6 shows the results of this analysis where the photon index is plotted against L_{HX}/L_{Edd}, where L_{HX} is computed using the unabsorbed flux in the 3.0–10.0 keV band.

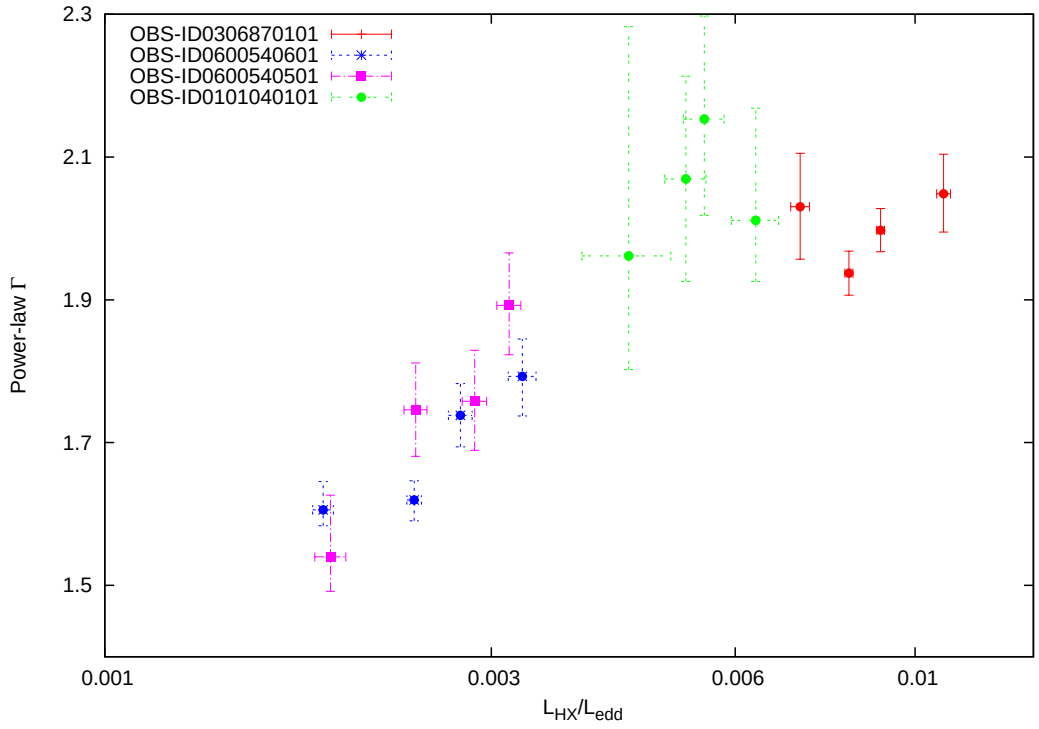

Figure 3.6: The high energy photon index, Γ versus the X-ray Eddington ratio for Mrk 335 in the energy range 3.0–10.0 keV is taken into account. The spectra are fitted with a power-law and Iron line. The similarity with Figure 3.5 implies that the qualitative results are not sensitive to the spectral model adopted.

Figure 3.7 shows the results of the flux resolved analysis (for the complete

0.3–10 keV band) for Ark 564. Here, despite the larger number of observations, the flux variation is modest with the X-ray Eddington ratio ranging from 0.2–0.7. Although there is more scatter than the case of Mrk 335, there is a correlation between the spectral index and X-ray Eddington ratio. A straight line fit gives a slope $m = 0.22 \pm 0.08$, intercept $c = 2.75 \pm 0.1$ and a large reduced $\chi^2 = 2.75$. From the Figure, it seems that for the flux resolved spectra of each individual observation the correlation may be better and perhaps the different observations are parallelly shifted with respect to each other. However, the statistics is not good enough to make any concrete statements.

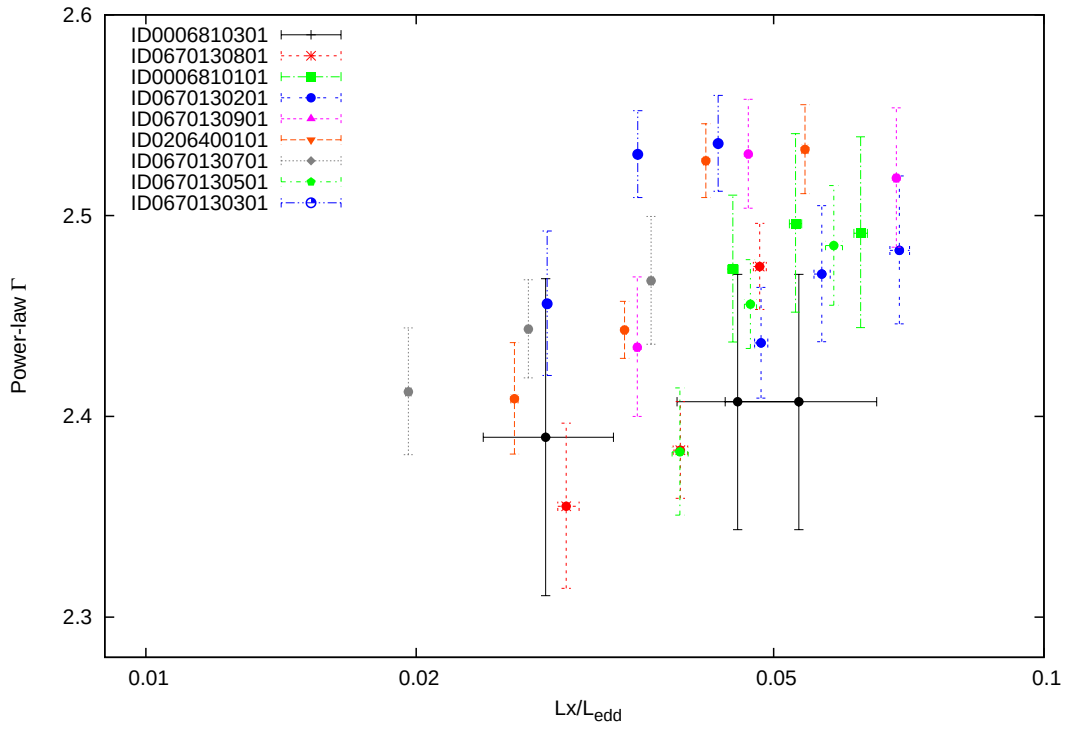

Figure 3.7: The high energy photon index, Γ versus the X-ray Eddington ratio for Ark 564. The X-ray Eddington ratio is L_X/L_{Edd} where L_X is the unabsorbed luminosity in the 0.3–10.0 keV range.

3.9 Discussion

Figure 3.8 summarises the results of the work by showing the variation of the high energy photon index versus the X-ray Eddington ratio for both Mrk 335 and

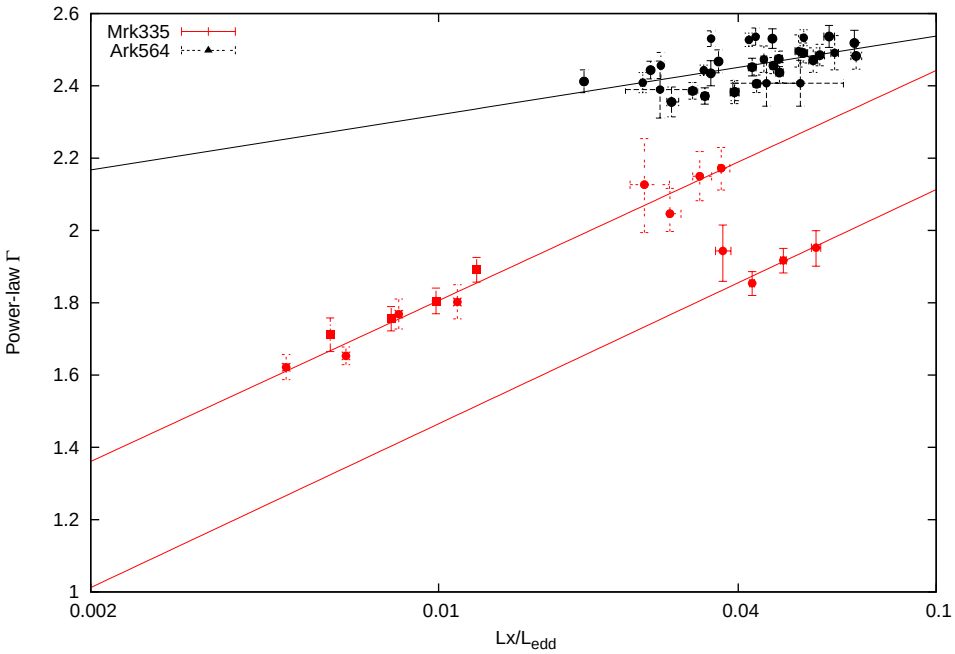

Figure 3.8: Summary figure for the high energy photon index, Γ versus the X-ray Eddington ratio for both Mrk 335 and Ark 564. The X-ray Eddington ratio is L_X/L_{Edd} where L_X is the unabsorbed luminosity in the 0.3–10.0 keV range.

Ark 564. For Mrk 335, there are two parallel tracks with the possibility that the sources shifts to the lower track for $L_x/L_{Edd} > 0.04$. For Ark 564 the points are clustered at a larger Γ and while there is a positive correlation, the slope is flatter and points show much more scatter than the points for Mrk 335.

It should be noted that the luminosity used in this work is in the energy range 0.3–10.0 keV and is not the bolometric one and hence these results cannot be compared directly with those where the bolometric luminosity or X-ray luminosity in some other energy range has been used. Since for Mrk 335, we find the the index correlates well with the X-ray luminosity for nearly an order of magnitude change in luminosity, this may indicate that over this range the bolometric correction is nearly constant. On the other hand, it may well be that for this source the X-ray index correlates better with the X-ray luminosity and not with the bolometric one. The uncertainties and model dependency of estimating the bolometric luminosity (including the general non-availability of simultaneous multi-wavelength data) does not allow for concrete statements. For Mrk 335, there

is only one observation for which the X-ray Eddington ratio is larger than 0.04 and the source follows a lower parallel track. It is necessary to confirm this behaviour with future observations when the source is equally luminous. It might be that there is a real transition at the X-ray Eddington ratio ~ 0.04 or that the source can actually follow any of the two tracks at the same luminosity.

In the Comptonization context, the high energy power-law index is inversely proportional to the Compton Amplification factor A, which is the ratio of the luminosity of Comptonizing cloud, L_c to the input soft photon luminosity L_{inp} i.e. $A = L_c/L_{inp}$. The input luminosity L_{inp} depends on the luminosity of the soft photon source and the fraction of photons which enter the Comptonizing region. The latter depends on the accretion geometry of the system. Thus, the correlation between the photon index and the observed luminosity could occur if A decreases with luminosity or in other words L_c varies less rapidly with the observed luminosity than L_{inp}. The shift to the lower parallel track can be explained if there is a decrease in L_{inp} at the X-ray Eddington ratio of ~ 0.04, perhaps caused by a change in the fraction of photons entering the Comptonizing region. This would mean that the accretion geometry for the two parallel tracks are different.

The high energy photon index could also be affected by the presence of a strong reflection component, especially if the reflection is from partially ionised matter and/or is relativistically blurred such that it has a significant contribution to the spectra below 10 keV. The reflection component would tend to flatten the high energy spectrum and hence the correlation may be caused by the reflection component decreasing as the source becomes more luminous. Indeed, the anomalous low luminosity observation of Mrk 335 of July 2007, can be modelled as being dominated by a blurred reflection component [297]. It may also be that the primary correlation between the index and luminosity is due to variation of the Compton Amplification factor, while the shift to a different parallel track is due to appearance of a strong reflection component. The appearance of a stronger reflection component would also mean that there was a change in the accretion disk geometry. Thus, a qualitative change in the accretion disk geometry seems to be required to explain the parallel tracks seen for Mrk 335. Note that in this analysis we have not included any reflection component, since there is no strong

residuals at high energies for our phenomenological fits and addition of a complex reflection would make our results model dependent, especially in the absence of high energy data. Changes in the accretion disk geometry at the same X-ray luminosity seems to indicate that the accretion flow is not determined only by the local accretion rate but rather it may also depend on the previous history of the accretion rate variation.

The results for Ark 564 are significantly different than that for Mrk 335, with a flatter correlation and more scatter. This suggests that the behaviour of AGNs is not homogeneous and perhaps cannot be understood by studying a large sample of them. Long term sensitive and broad band monitoring of individual AGNs may be expected to provide better insights.

3.10 Summary

The *XMM-Newton* observations of Mrk 335 and Ark 564 reveals

• The variation of the high energy photon index versus the X-ray Eddington ratio for both Mrk 335 and Ark 564 have been studied and it is found that for Mrk 335, there are two parallel tracks with the possibility that the sources shifts to the lower track for L_x/L_{Edd} >0.04.

• For Mrk 335, three of the observations (0600540601, 0600540501 and 0101040101) cover an order of magnitude range in X-ray Eddington ratio from 0.004 to 0.04 and show a tight correlation between the photon index and X-ray Eddington ratio. A straight line fit gives a slope $m = 0.64 \pm 0.04$, intercept $c = 3.08 \pm 0.08$ and reduced $\chi^2 = 0.57$.

• The flux resolved spectra for observation with the highest X-ray Eddington ratio > 0.04, one gets a straight line with slope $m = 0.65 \pm 0.04$, intercept $c = 2.76 \pm 0.07$ and reduced $\chi^2 = 0.76$.

• For Ark 564 also there exist a correlation which is flatter and scatter than Mrk 335 between photon index and the X-ray Eddington ratio.

⋆ ⋆ ⋆